

## 5. Metal Ultradispersion

---

---

<b>5. Metal Ultradispersion</b>	<b>265</b>
<b>5.1 Introduction</b>	<b>267</b>
<b>5.2 Experimental Details</b>	<b>269</b>
5.2.1 Electroless Method	269
5.2.2 Microwave Method	270
5.2.3 Analytical Techniques Used	271
5.2.4 Ex-situ Reduction Treatments	271
5.2.5 In-situ Reduction Treatments	272
<b>5.3 Ultradispersed Distributions – Low Pd Loadings</b>	<b>273</b>
5.3.1 Sample As-grown – Before Reduction Processes	273
5.3.2 Sample after the Ex-situ Reduction Treatment	278
5.3.3 Sample after the In-situ Reduction Treatment	281
<b>5.4 From ultradispersion to surface nucleation – High Pd loadings</b>	<b>285</b>
5.4.1 Sample Nanostructure Before Reduction	285

---

5.4.2 Sample Nanostructure After Reduction	291
5.4.2.1 Stick-like SnO <sub>2</sub> Nanoparticles Structure	293
5.4.2.2 Palladium Clusters and Tin Oxide Nanosticks Epitaxy	297
5.4.2.3 Metal Nanoclusters Morphology	303
5.4.3 Structural influence on the Electrical Sensing Response	308
<b>5.5 Conclusions</b>	<b>313</b>
<b>References</b>	<b>316</b>

### 5.1 Introduction

As it is well known [1, 2] and as we have also shown in recent works [3], palladium loaded on SnO<sub>2</sub> nanoparticles can be atomically ultradispersed on semiconductors surface. The aim of this *Chapter* is to study the catalytic metal ultradispersion as another of the last, but not the least, example of possible catalytic distribution ways. Therefore we have selected Pd/SnO<sub>2</sub> systems as a good example of such a noble metal distribution. We are especially interested in following the evolution of palladium atoms from monoatomic ultradispersion, in the case of low palladium loadings, to metal clustering, for high palladium loadings. In this way, we will apply the techniques introduced in *Chapter 2*, as HRTEM related techniques, ICP and XRD, in order to follow the mentioned evolution.

The *Chapter* will be divided in two main parts. In the first one (*Section 5.3*), we will study samples loaded with low Pd wt. % percentage (< 2 wt. %), for which palladium is expected to be ultradispersed. In this way, we prepared several samples by the electroless method, which let us to accurately control the introduction of low palladium doses. As ultradispersed Pd atoms can not be imaged using HRTEM techniques, we have submitted SnO<sub>2</sub> samples impregnated with Pd to both in-situ and ex-situ reduction treatments in order to nucleate the dispersed atoms in observable surface nanoclusters. The ex-situ reduction treatments consisted in heating the sample under Ar atmosphere with 5% of H<sub>2</sub>, whereas the in-situ reduction consisted in focussing the microscope's electron beam at 300 kV over a reduced area of the sample. On the samples treated ex-situ, we have obtained HRTEM micrographs showing the effects of reduction in a hydrogen atmosphere (transformation of SnO<sub>2</sub> into SnO in localised patches as well as nucleation of Pd nanoclusters). On the in-situ reduced sample, we could

additionally obtain HRTEM micrograph sequences showing the reduction process in real-time.

The second part of the chapter (*Section 5.4*) has been devoted to achieve a complete analysis of SnO<sub>2</sub> samples with high palladium wt. % loading. In this case, samples have been obtained by the microwave method, since this method has been found to give extremely good results for high percentage noble metal loadings. As we will describe in the following, high Pd loadings allow the nucleation of surface nanoclusters as in the former case shown in *Chapter 4* (Pt/TiO<sub>2</sub>). The samples have been studied before and after ex-situ reduction process, which allows us to study the morphological and structural effects of reducing environments during gas sensing. Moreover, we have also studied the epitaxial relationships between metal clusters and semiconductor support using supercell models and their corresponding computer simulations. The presence of epitaxial or no epitaxial growth between metal cluster and substrate depending on the palladium reduction state will be also discussed in terms of charge interchange during gas sensing.

### 5.2 Experimental Details

In the following, we will describe the sample preparation methods used, such as the innovative variation of the electroless method and the microwave method, both developed in our Department.<sup>♦</sup> Moreover we will describe the ex-situ and in-situ reduction processes that have helped us during sample analysis.

#### 5.2.1 Electroless Method

As it is well known, the sensitivity and selectivity of a SGS material also depend on the procedure to obtain it [4]. This dependence is influenced by the morphological and structural changes that every method can induce to the resultant material. In this *Section*, and in order to obtain a good ultradispersion of palladium atoms, we used an improved version of the electroless method [5]. With this method we can obtain catalyzed tin oxide and we can control with high precision the introduction of low noble metal doses. Electroless metal deposition processes have been widely used since their introduction by Brenner and Riddell [6] to provide metal coating of surfaces by simple immersion in a suitable aqueous solution. Its principles and behavior are well established [7] and, thus, metal deposition is obtained by reduction of metal ions present in the solution by means of a chemical reducing agent. The advantages of the proposed technique are high reliability and repeatability, mass production implementation facilities and low-cost

---

<sup>♦</sup> The variation of the electroless method used to prepare the low loaded Pd/SnO<sub>2</sub> samples, was developed by R. Díaz in a collaboration work between Dept. d'Electrònica and Dept. de Química-Física of UB. On the other hand, the microwave method used for high Pd loadings, was developed by A. Cirera in our own department (Electrònica).

production. Nevertheless, this electroless process has been scarcely used for the Palladium addition and a two-step Palladium addition process is the classical electroless process [8]. Thereby, SnO<sub>2</sub> nanopowders are catalyzed with palladium coming from a solution containing PdCl<sub>2</sub> and are deposited via a single-step electroless process with SnCl<sub>2</sub> acting as reductor. Different metal salt and reductor concentrations in the solution are used to study the influence of these parameters on the final catalyst concentration of SnO<sub>2</sub>. The preparation of catalyzed tin oxide has been made adding an SnO<sub>2</sub> powder to a PdCl<sub>2</sub> aqueous solution 5·10<sup>-3</sup> M in HCl (since acid enables the palladium salt solution process, we choose the proposed solution to have anytime an excess of the acid with respect to the different palladium concentrations studied). The solution is then rinsed in a Memmert model WB14 bath provided with a M00 rinsing machine, thus obtaining a solid suspension of the SnO<sub>2</sub> powder in the catalyst solution. The temperature (30 °C) and the rinse rate were maintained during 15 minutes just to achieve the thermal equilibrium. Then, a freshly prepared aqueous solution of SnCl<sub>2</sub> is added and the whole solution is rinsed at the same temperature and rate during 50 minutes. The nominal atomic Pd/Sn ratios used have been 1-5% in atomic concentration (0.71-3.53% Pd/SnO<sub>2</sub>). Afterwards, a filtration using Albet model 420 filters is released, rinsing with diluted HCl and then with water. A final desiccation process at 80 °C was done to collect the final powder. Then, a thermal treatment is applied. This treatment consists in a 8 hours heating at 800 °C, reached with a rate of 20 °C min<sup>-1</sup>. Products used are: PdCl<sub>2</sub>(99.9%), SnCl<sub>2</sub>(99%) and SnO<sub>2</sub>(99.9%) (all from Alfa) and HCl(37% fuming) from Merckx.

### 5.2.2 Microwave Method

We selected this innovative method as it had been widely demonstrated in previous works [3, 9, 10], that it has a good efficiency for high noble metal loading. As introduced in *Chapter 1*, this procedure consists in the irradiation with 2.45 GHz microwaves of a solution

## 5. Metal Ultradispersion

---

containing tin oxide plus the chloride compounds of the catalytic additives. After this process we obtain pseudo-crystalline tin oxide with the added noble metal, resultant material that needs to be stabilized. In our case, the tin oxide precursor used was  $\text{SnCl}_4 \cdot 5(\text{H}_2\text{O})$ , while the palladium precursor used was  $\text{PdCl}_2$ , in a nominal atomic concentration of 10% Pd/Sn (7.06 Pd/ $\text{SnO}_2$  wt.%).

In a last process, we applied a 600 °C thermal annealing on our materials during 8 hours in order to stabilize our material. These thermal treatments are also usual in other technologies as sol-gel [11].

### 5.2.3 Analytical Techniques Used

Both structural (HRTEM, TEM and XRD) and chemical characterization techniques (ICP) have been used to analyze the sensing powders. Further description of these techniques has been carried out in *Chapter 2*. With respect to the ICP analysis, the knowledge of the analysis process is useful for the results presented below. Following the three steps described in *Chapter 2* for the ICP spectroscopic measurements, we can subtract accurately our specimen composition, and furthermore, we can find where the catalytic loaded was placed (in or outside the semiconductor material).

### 5.2.4 Ex-situ Reduction Treatments

The ex-situ reduction treatments were carried out following the procedure reported by S. Bernal and co-workers elsewhere [12]. The procedure consists of heating the Pd/ $\text{SnO}_2$  sample in a flow of 5%  $\text{H}_2$  /Ar gas mixture (60  $\text{cm}^3/\text{min}$ ) at 10  $\text{K min}^{-1}$  from room temperature (298 K) to the selected reduction temperature (473 K). The samples were held for 2 h at the reduction temperature, then treated in flowing helium (60  $\text{cm}^3/\text{min}$ ) for 1 hour at the reduction temperature and, finally, they were cooled, also in a flow of inert gas. To prevent the fast reoxidation of the reduced catalysts, samples were cooled to 191 K, always in flow of helium, then treated with

O<sub>2</sub> (5%)-He for ½hour, warmed to 295 K in the oxidizing mixture and finally exposed to air.\*

### 5.2.5 In-situ Reduction Treatments

For the in-situ reduction, the microscope's electron beam, at 300 kV, was focussed over tiny areas of the sample. As suggested by Suzuki et al [13], overheating of SnO<sub>2</sub> samples while focussing the electron beam on a small region induces material evaporation during the period of observation. The energy transferred by the electrons to the material promotes the breakage of Sn-O bonds, what leads the SnO<sub>2</sub> crystallites to evaporate slowly during irradiation. We will use this a priori undesirable effect to obtain a pseudo-reduction on our samples, with the advantage that the process can be recorded in real-time.

---

\* The ex-situ reduction treatments were carried out in Departamento de Ciencia de los Materiales, Ingeniería Metalúrgica y Química Inorgánica of Universidad de Cádiz, Spain.

### 5.3 Ultradispersed Distributions – Low Pd Loadings

In the following *Section* we will analyze the affinity of palladium atoms to remain ultradispersed on SnO<sub>2</sub> particle surface. Both, in-situ and ex-situ reduction methods will be used in order to nucleate the palladium atoms in HRTEM observable clusters. Real-time sequential images have been obtained for the in-situ reduction process to show the steps followed during nucleation. Digital Image Processing (DIP) will be applied to HRTEM micrographs to analyze the small nanoclusters formation after reduction treatments.

#### 5.3.1 Sample As-grown – Before Reduction Processes

In the following, we will show the compositional and structural characteristics of the as-grown electroless samples with low nominal palladium wt.% loading (from 0.71 to 3.53 Pd/SnO<sub>2</sub> wt.%).

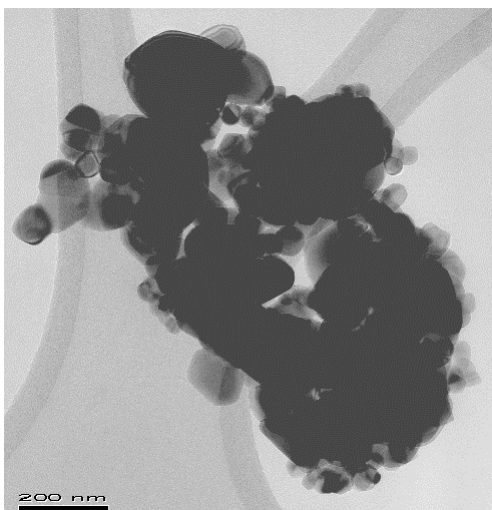


**Figure 5.1.** General TEM view of the SnO<sub>2</sub> nanopowders for the sample grown by the electroless method with low Pd wt.% loading.

As shown in *figure 5.1*, the SnO<sub>2</sub> nanoparticles present rounded shapes. In this case, the sample imaged corresponds to the 3.53 wt.% palladium loading. There is not a homogeneous particle size distribution, since their sizes range from 30 to 300 nm in diameter. As a result of

their size inhomogeneity, it is not possible to obtain a mean diameter.

A more detailed analysis is made in the HRTEM image shown in *figure 5.2*. The micrograph shows a pure tin oxide nanoparticle as deduced from DIP study. The particle was imaged in the [001] zone axis and shows clearly the {100} and {110} family planes (see also *table 5.1*). After results obtained for Pt/TiO<sub>2</sub> samples in *Chapter 4*, we would expect to find a big amount of palladium nanoclusters on SnO<sub>2</sub> particles surface for such a loading value, if palladium followed the same nucleation behavior as platinum. Surprisingly, the presence of palladium nanoclusters on SnO<sub>2</sub> surface is not as high as in Pt/TiO<sub>2</sub> systems for similar noble metal wt.% loadings. As shown in *figure 5.3*, few metal clusters (mainly in their oxidized form, PdO) have been found in the Pd/SnO<sub>2</sub> samples grown by the electroless method for palladium loadings lower than 3.53 wt.%. Moreover, these nanoclusters are not homogeneously distributed and can be hardly found. As the structure of SnO<sub>2</sub> has not been modified in nanoparticles bulk, we can also suggest that palladium atoms do not form a complex oxide alloy with tin. If the main part of Pd atoms does not nucleate in surface nanoclusters and does not compose a mixed oxide with tin, then these atoms

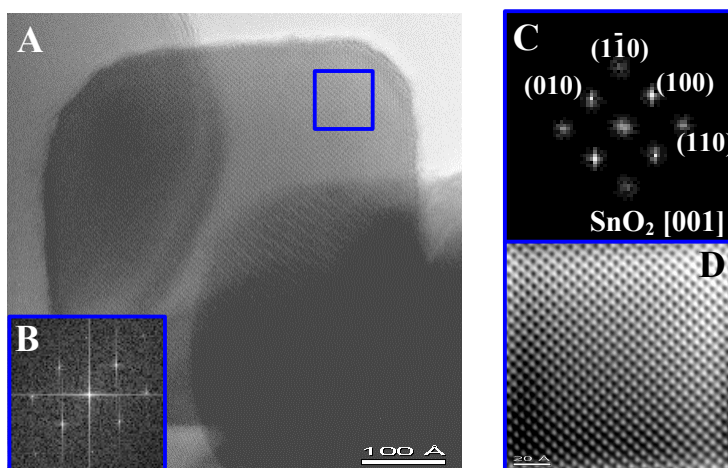


**Figure 5.2.** (a) HRTEM micrograph of one of the as-grown SnO<sub>2</sub> nanoparticles for the electroless sample with low Pd wt.% loading (3.53 wt.%). (b) FFT of the squared area in (a). (c) Mask filtering of the FFT in (b). (d) Inverse FFT of the filtered spots in (c). Atomic planes are visualized in [001] zones axis.

## 5. Metal Ultradispersion

could be placed in ultradispersed way on SnO<sub>2</sub> surface. This result is extensive to the rest of samples grown by the electroless method with lower nominal Pd wt. %.

Plane 1	Plane 2	D1 (Å)	D2 (Å)	Angle	Zone Axis
(100)	(110)	4.74	3.35	45.0 °	[001]
(100)	(010)	4.74	4.74	90.0 °	[001]
(1-10)	(110)	3.35	3.35	90.0 °	[001]
(01-1)	(10-1)	2.64	2.64	46.5 °	[111]
(1-10)	(10-1)	3.35	2.64	66.8 °	[111]
(1-11)	(001)	2.31	3.19	43.6 °	[110]
(1-11)	(1-10)	2.31	3.35	46.4 °	[110]
(-111)	(1-11)	2.31	2.31	87.1 °	[110]
(001)	(1-10)	3.19	3.35	90.0 °	[110]

**Table 5.1.** Angle and distance plane relationship for SnO<sub>2</sub> rutile phase [14].

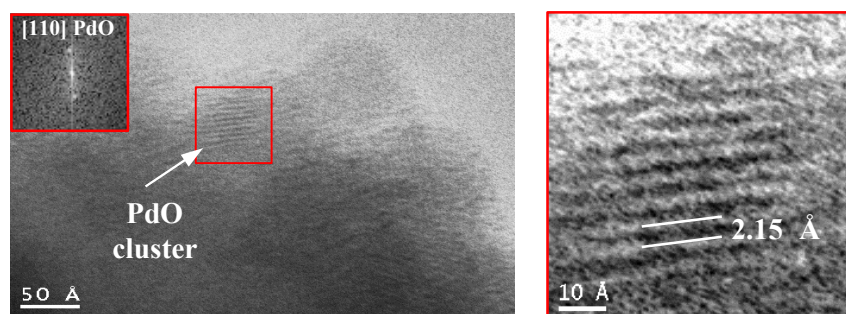


**Figure 5.3.** HRTEM micrograph of the as-grown sample with 3.53 wt.% palladium loading. A PdO nanocluster is squared. DIP shows that cluster atomic planes showed in the image correspond to the (110)<sub>PdO</sub>.

In the following, we have used the ICP protocol explained in *section 5.2.3*, in order to estimate the compositional characteristics of one of the samples studied.

Nominal Pd/SnO <sub>2</sub> (wt. %)	Annealing T (°C)	Pd found	Pd solubilized In the 1 <sup>st</sup> step (%)	Pd solubilized In the 3 <sup>rd</sup> step (%)
3.53	800	1.69 Pd/SnO <sub>2</sub> wt.%	0.34 Pd/SnO <sub>2</sub> wt. % (20 %)	1.35 Pd/SnO <sub>2</sub> wt. % (80 %)

**Table 5.2.** ICP results for the sample with the highest catalytic nominal percentage grown by the electroless method.

Results shown in *table 5.2* can help to clarify palladium atoms behavior when they act as catalytic in tin oxide systems. First of all, we should notice that the real palladium wt.% is approximately half (48%) of the loaded nominal value. This means that we lose half of the catalytic atoms during the first stages of sample preparation and that the final equivalent loading is of about 1.69 wt.%. Anyway, it is important to understand the meaning of palladium solubilized in the 1<sup>st</sup> and 3<sup>rd</sup> steps of ICP techniques.

In the first step, all catalytic aggregates present on SnO<sub>2</sub> surface are solubilized. This means that the 20 wt.% of the total Pd found in our sample was present on SnO<sub>2</sub> surface as metal (Pd) or oxide clusters (PdO). Taking into account the palladium losses, we obtain that just a 0.34 wt.% of the sample is palladium forming surface aggregates, this can explain the low number of palladium clusters found on SnO<sub>2</sub> surface on the HRTEM analysis. During the second step, we solubilize tin oxides; thus the solid metal species remaining after the second step will be solubilized during the third step. After new ICP analysis of the last solution, we obtained that 80 % of the total palladium found in the sample had been solubilized during the third step. This 80% corresponds to the 1.35 Pd/SnO<sub>2</sub> wt.%.

It is clear that palladium atoms solubilized during the first stage were those forming surface aggregates. What it is not so clear is the placement in our SGS samples of the palladium atoms found after the third solubilization stage. It is possible to consider that these palladium atoms were initially ultradispersed on SnO<sub>2</sub> surface, and directly bonded to surface oxygen. Then, during the first solubilization, all the ultradispersed palladium atoms would remain bonded to the surface O over SnO<sub>2</sub> and wouldn't be

## 5. Metal Ultradispersion

---

detected by the ICP immediate analyses. In the second step, when all tin oxide species are solubilized, this would promote the breakage of Pd-O surface bonds leading the Pd detection after the 3<sup>rd</sup> solubilization process. In this way, results found by Matsushima and co-workers in a recent work [15] are in good agreement with our suggestion. In their study, they showed the affinity of palladium atoms to the direct chemical bonding, with both covalent and ionic character, with surface O in SnO<sub>2</sub>. In one of the models shown in their work they found that Pd bonding with surface O is purely atomic-like (model was shown in *section 1.3.2.3*). Furthermore, some other works found in literature [1, 2], also suggest the atomic-like ultradispersion of palladium atoms on SnO<sub>2</sub> semiconductors surface. All these results found seem to be in good concordance with our considerations.

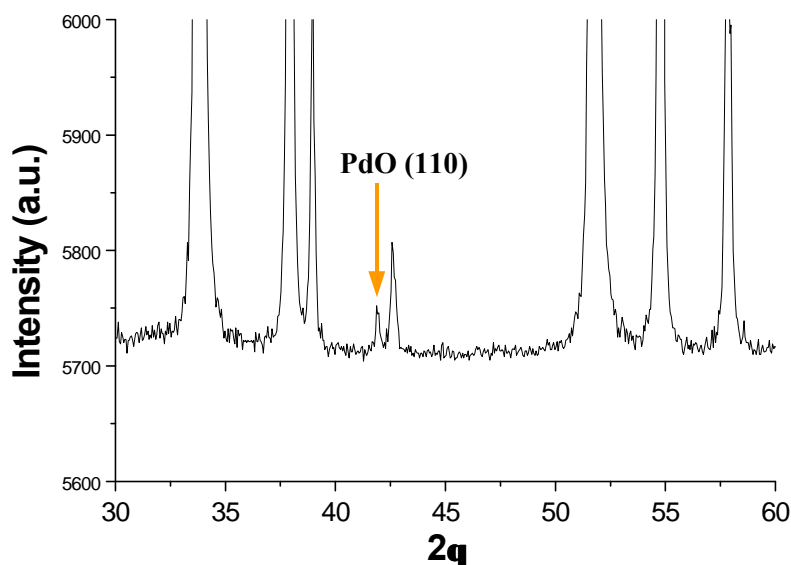


**Figure 5.4.** XRD spectra of the as-grown nanopowders with 3.53 wt.% Pd loading. The main part of the peaks corresponds to SnO<sub>2</sub>. The marked peak corresponds to the (110) PdO planes.

Further analysis on the as-grown samples carried on by XRD, corroborates that our material is composed by pure SnO<sub>2</sub> crystallites. In *figure 5.4*, we show the XRD spectra of the as-grown SnO<sub>2</sub> nanopowders with 3.53 wt.% nominal palladium loading. All the peaks present in the

spectra correspond to the SnO<sub>2</sub> cassiterite structure, except the one marked with an arrow, which corresponds to the (110) PdO planes. We attribute the small PdO peak to the palladium forming surface aggregates or clusters. In this case, palladium clusters would be completely oxidized in the as-grown samples, as shown in the XRD spectra and as we have found using HRTEM DIP analysis. The small height of the PdO peak suggests that percentage of palladium atoms composing the aggregates is low, in good agreement with results obtained by ICP where just a 0.34 wt.% of palladium was found to nucleate on surface. The rest of palladium atoms, those atomically ultradispersed on SnO<sub>2</sub> surface, can not be detected using XRD, as they do not have a crystalline structure.

In order to visualize ultradispersed atoms we have submitted our samples to in-situ and ex-situ reduction experiences. With these treatments, we expect to provide the palladium atoms with energy enough to nucleate (sinter) in small nanoclusters. In the following *Sections* we will show these results.

### 5.3.2 Sample after the Ex-situ Reduction Treatment

We have submitted the sample with 3.53 Pd/SnO<sub>2</sub> wt.% grown by the electroless method to an ex-situ reduction treatment at 473 K. By comparing the HRTEM micrographs obtained before and after the reduction process (compare for example *figures 5.2* and *5.5*), we find that small hills decor the SnO<sub>2</sub> nanoparticles after reduction. A detailed analysis of these hills is made in *figure 5.6*. We find that the basis of the hill is composed by tin monoxide (SnO) while small palladium nanoclusters are embedded on the top of these hills (see *tables 5.3* and *5.4*, respectively). The density of these Pd clusters is far higher than that found before reduction, suggesting that the main part of this nanoclusters are the result of ultradispersed palladium atoms nucleation (sintering) due to the reduction process. Other authors have also observed metal sintering when submitting noble metal catalysts to a reduction treatment. In this way, Cubeiro et al. [16], observed that pretreatments of the Pd/ZnO catalysts in hydrogen at 573 K led to

## 5. Metal Ultradispersion

---

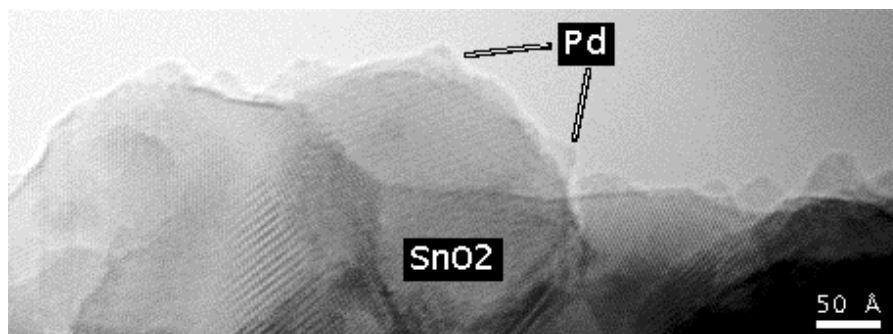


**Figure 5.5.** HRTEM micrograph of the electroless sample with low Pd loading after ex-situ reduction at 473 K. Nucleation of Palladium nanoclusters is obtained on the top of the reduced tin oxide nanopowders.

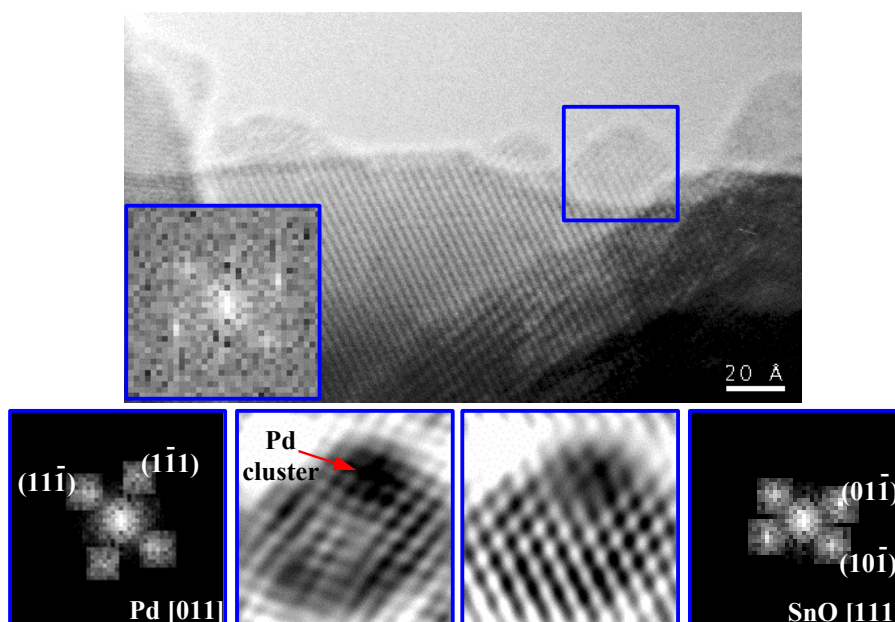


**Figure 5.6.** Detailed analysis of a Pd nanocluster after reduction at 473 K. The small hills that decor SnO<sub>2</sub> particles surface are in fact SnO as a consequence of the reduction treatment. Pd nanoclusters seem to nucleate on the top of these SnO hills.

sintering of metallic particles. Lomot and co-workers [17], also observed a considerable sintering of palladium after reduction of Pd/Al<sub>2</sub>O<sub>3</sub> systems in H<sub>2</sub> and He gas flow mixture at 873 K. The sintering effects of palladium in the former works it is clear, however they used in their treatments higher

temperatures than us. We also wanted to improve metal sintering by increasing reduction treatment temperatures, but we found that SnO<sub>2</sub> is highly reactive in front of H<sub>2</sub> treatments, and this reactivity is increased when increasing the temperature. We tried to submit our samples to a reduction process at 873 K and we found that the SnO<sub>2</sub> was completely reduced. The resultant species we found were Sn in its metallic phase mixed with Pd. After this attempt we discarded reduction processes at high temperatures and we just worked with treatments at 473 K, which at least assured a good reduction of Pd species and a slight metal sintering. Mastalir et al. [18], also worked in the range of temperatures from 323 to 573 K with Pd-Graphimet catalysts, finding that the effects of reduction processes were far more pronounced at high temperatures where all the inserted Pd atoms underwent migration and a sintering of the surface Pd crystallites took place. Nevertheless, they found that at temperatures as low as 323 K some palladium sintering could be also appreciated.

The origin of the new Pd clusters that appeared on the top of the SnO reduced hills seems to be the metal sintering induced by reduction treatments.

Plane 1	Plane 2	D1 (Å)	D2 (Å)	Angle	Zone Axis
(01-1)	(10-1)	2.76	2.86	64.7 °	[111]

**Table 5.3.** Angle and distance plane relationship for SnO reduced phase.

Plane 1	Plane 2	D1 (Å)	D2 (Å)	Angle	Zone Axis
(200)	(020)	1.95	1.95	90.0 °	[001]
(1-11)	(11-1)	2.25	2.25	70.5 °	[011]
(200)	(11-1)	1.95	2.25	54.7 °	[011]

**Table 5.4.** Angle and distance plane relationship for Pd metallic phase.

### 5.3.3 Sample after the In-situ Reduction Treatment

In order to observe in-situ the reduced hills formation and metal sintering, we carried out the novel experience described in *Section 5.2.5*, and reported in recent works [3].

The energy transferred by the electrons to the material promotes the breakage of Sn-O bonds, what leads the SnO<sub>2</sub> crystallites to evaporate slowly during irradiation. As shown in *figure 5.7*, particle size decrease takes place as a consequence of this process, as well as the growth of hills on nanoparticle surface. A more detailed analysis of particle morphology is made in *figures 5.8, 5.9 and 5.10*.

In *figure 5.8*, we used DIP in order to determine the morphology and chemical structure of the particle selected. The digital diffractogram of the squared area reveals that the nanoparticle is composed of pure SnO<sub>2</sub>. In this case, the particle has been imaged in the [001] zone axis. The micrograph has been taken during the first stages of the in-situ reduction process, when no effects can be still appreciated. It should be noticed that nanoparticle surface remains clean with no presence of reduced hills or Pd nanoclusters.

In *figure 5.9*, we show the evolved SnO<sub>2</sub> nanoparticle in an advanced step of the in-situ reduction process. Several corrugations or hills decor the SnO<sub>2</sub> surface. Results shown are similar to those obtained after the ex-situ reduction processes. In this case, a detailed analysis of one of the hills (*Figure 5.10*) shows that palladium nucleation occurred. DIP allows as to separate SnO<sub>2</sub> phase information from that corresponding to Pd. As it happened before, during the ex-situ processes, Pd atoms, which were initially ultradispersed over SnO<sub>2</sub> surface acquires energy enough to nucleate and grow in the form of nanosized clusters. Since we could not observe palladium nanoclusters on the surface of SnO<sub>2</sub> before this in-situ pseudo-reduction, the process carried out demonstrates that palladium atoms were placed in an ultradispersed way over the SnO<sub>2</sub> surface before the irradiation process.

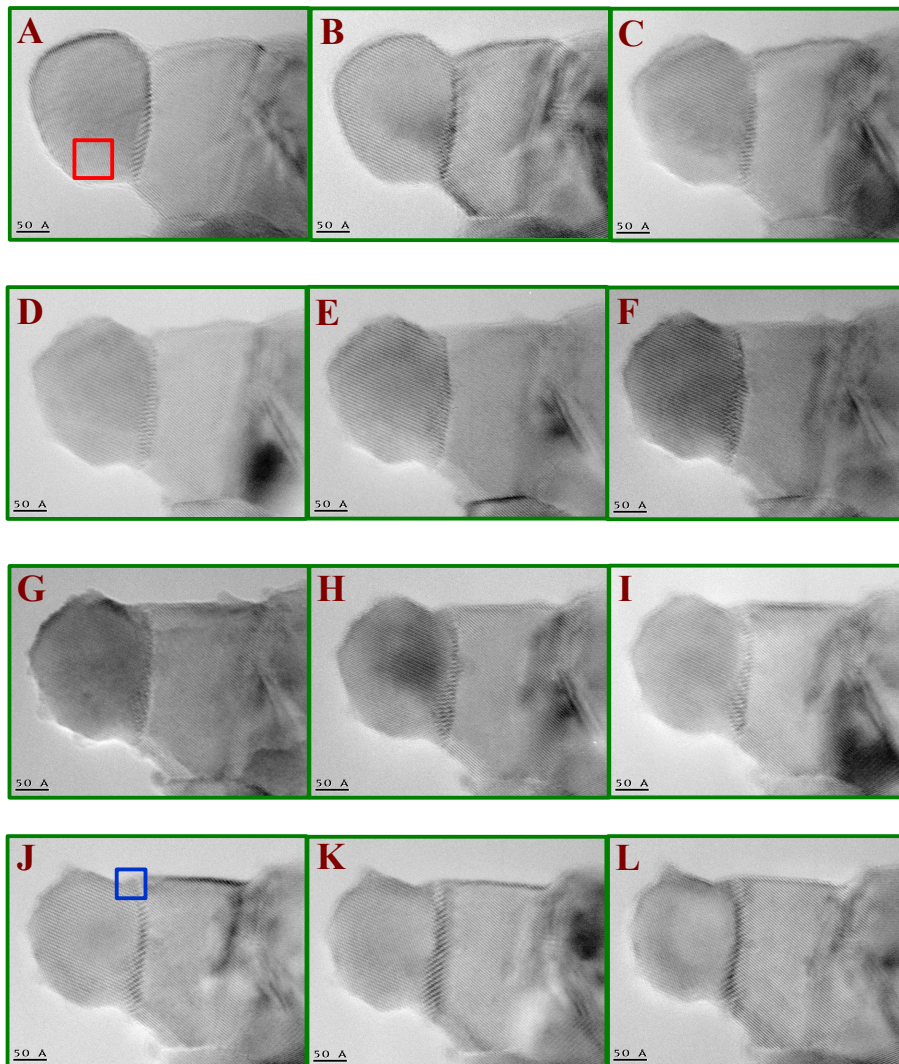


**Figure 5.7.** Temporal Map of HRTEM micrographs obtained during the in-situ reduction of the electroless sample with low Pd concentration. Notice how there is a diminution of the SnO<sub>2</sub> particle size due to material evaporation. Electron beam provides the necessary energy to Pd atoms to nucleate on SnO<sub>2</sub> surface.

## 5. Metal Ultradispersion

---

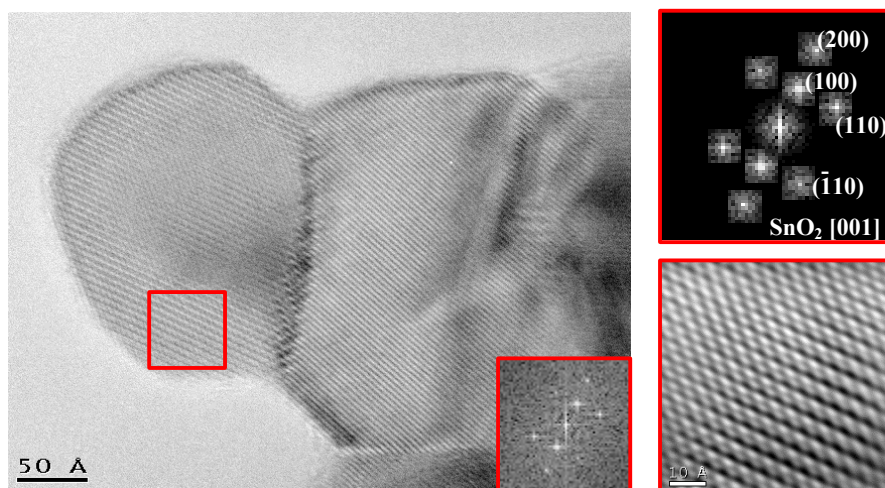


**Figure 5.8.** HRTEM micrograph of the electroless sample with low Pd loading, just before the in-situ reduction. There is no evidence of Pd surface clustering, nanoparticles are composed of pure SnO<sub>2</sub>.

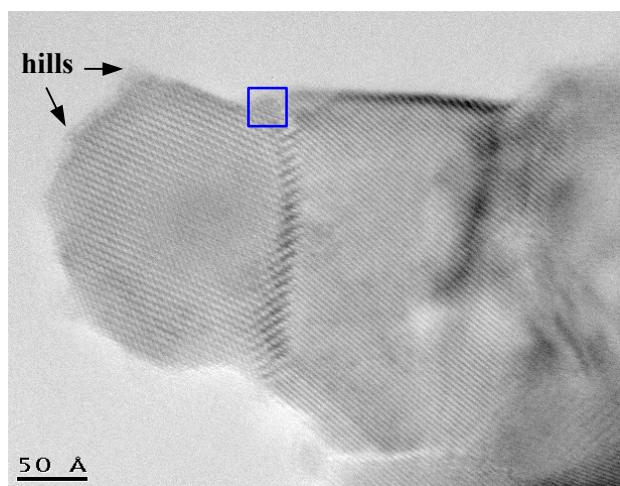


**Figure 5.9.** HRTEM image corresponding to the electroless sample with low Pd loading. The micrograph was taken during the in-situ reduction process. Notice that the formation of reduced hills on SnO<sub>2</sub> particle surface is similar to effects of the ex-situ process.

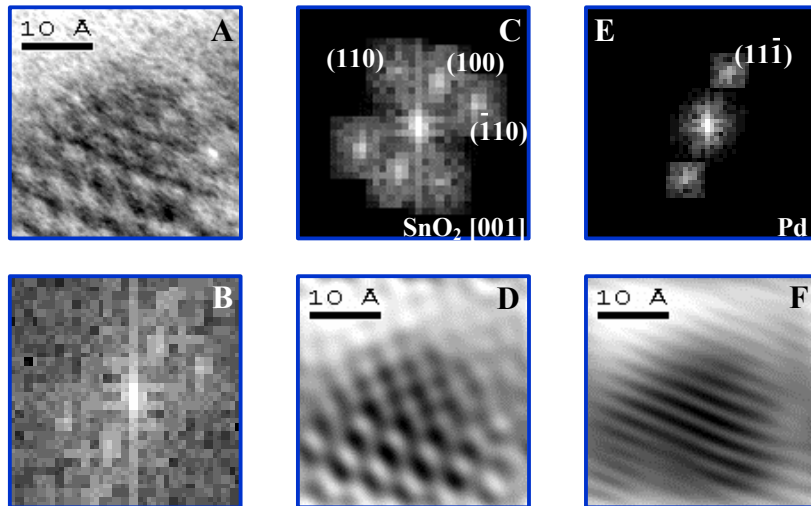


**Figure 5.10.** (a) High magnification detail of the area squared in *figure 5.9*. (b) FFT of the image in (a). (c) Mask filtering of the FFT in (b) corresponding to SnO<sub>2</sub> frequency data. (d) Inverse FFT of the filtered spots in (c). (e) Mask filtering corresponding to the palladium (11-1) plane frequency. (f) Inverse FFT of mask showed in (e).

### 5.4 From ultradispersion to surface nucleation – High Pd loadings

In the following, we will achieve a complete analysis of SnO<sub>2</sub> samples with high palladium loading (7.06 wt.%). Samples have been prepared by the microwave method, since this method has been found to give good results for high percentage noble metal loadings [19]. The samples will be studied before and after ex-situ reduction process. We will focus our efforts specially on determining the morphological and structural effects of reducing environments during gas sensing. Moreover, we will also study the epitaxial relationships between metal clusters and semiconductor support using supercell models and their corresponding computer simulations. The presence or non-presence of an epitaxial relationship between metal cluster and substrate depending on the palladium reduction state will be also discussed in terms of charge interchange during gas sensing.

#### 5.4.1 Sample Nanostructure Before Reduction

A general TEM view of the as-grown sample is shown in *figure 5.11*. Big agglomerations of nanoparticles can be observed, as well as some other dispersed grains. Notice that some of the SnO<sub>2</sub> nanoparticles adopt a curious rectangular prism shape (like sticks). This stick-like structure wasn't observed before in other samples with lower Pd loading, even in those prepared by the microwave method. We could a priori think, that those sticks could be composed of some other material different from SnO<sub>2</sub>. That is the case, for example, of the presence of stick-like particles in BaSnO<sub>3</sub> nanopowders, where the prism particles have been found to be composed of

BaCO<sub>3</sub> instead of BaSnO<sub>3</sub> [20]. In the later case, BaCO<sub>3</sub> formation is due to atmospherical contamination interaction with the annealed material.

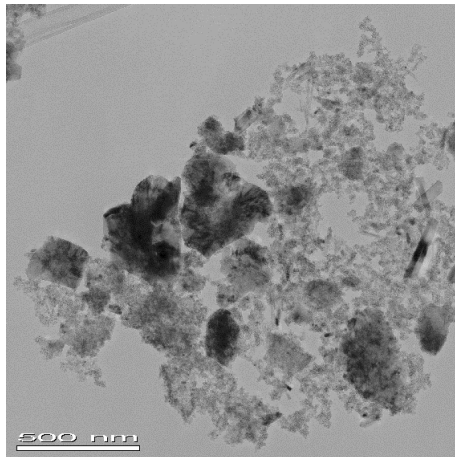


**Figure 5.11.** General TEM view of the sample prepared by the microwave method with high Pd wt.% loading. Sample as-grown, before reduction.

In this way, and in order to obtain its nanostructure, a more detailed analysis of one of these prism particles has been carried out. In *figure 5.12*, we show a HRTEM micrograph of one of these stick-like nanoparticles. In the right side of the *figure* we also show a magnified detail of a selected region from the stick-like nanoparticle. The atomic planes are perfectly shown and the corresponding atomic structure analysis confirms that these particles are also composed of

pure SnO<sub>2</sub>, as obtained after DIP. In our case, the presence of a high palladium percentage could influence the SnO<sub>2</sub> growing, determining the

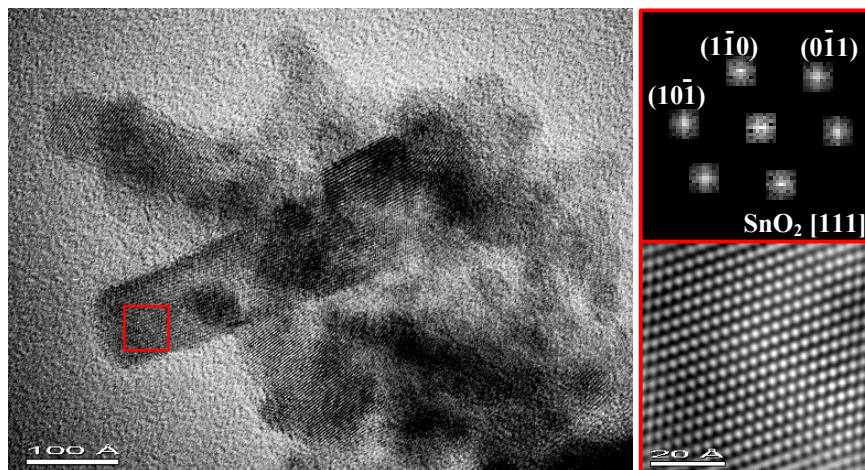


**Figure 5.12.** HRTEM micrograph of the SnO<sub>2</sub> nanoparticles, some of them adopt rectangular prism shape (like sticks). On the right side we show a magnified filtered detail extracted from the squared area. Sticks are composed of pure SnO<sub>2</sub>.

## 5. Metal Ultradispersion

---

faceting of the rutile nanoparticles in the observed faces during the growth steps. This influence has been demonstrated by comparing the morphology of these stick-like nanoparticles obtained at high Pd loadings with those SnO<sub>2</sub> nanopowders obtained at low Pd loadings, where SnO<sub>2</sub> nanoparticles have quasi-spherical shapes and there is no presence of the prism nanoparticles [10].

A general detection of the nanopowders phases has been made using SAED patterns. In *figure 5.13* we show one of the SAED patterns obtained for our high palladium loading sample before reduction. A profile analysis has been carried out in order to determine the crystalline composition of the sample. As shown in *table 5.5*, the different rings and spots visualized in *figure 5.13* SAED pattern, correspond to SnO<sub>2</sub> and PdO.

# Ring	d (Å)	plane	phase
1	3.35	(110)	SnO <sub>2</sub>
2	3.05	(100)	PdO
3	2.64	(101)/(101)	SnO <sub>2</sub> /PdO
4	2.37	(200)	SnO <sub>2</sub>
5	2.31	(111)	SnO <sub>2</sub>
6	2.15	(110)	PdO
7	1.76	(211)	SnO <sub>2</sub>
8	1.68	(112)	PdO

**Table 5.5.** SAED pattern profile indexation corresponding to that shown in *figure 5.13*, for sample as-grown.

The presence of slight rings corresponding to the palladium oxidized phase (PdO), and the absence of metallic palladium information in SAED patterns, shows that in the as-grown sample the main part of Pd atoms nucleate forming small structures (possibly nanoclusters) in their oxidized phase. The presence of the PdO structures instead of the metallic ones (Pd) in the as-grown catalysts, has been extensively reported in literature [21, 22, 23]. It is important to notice that while Pt has been mainly found as metallic

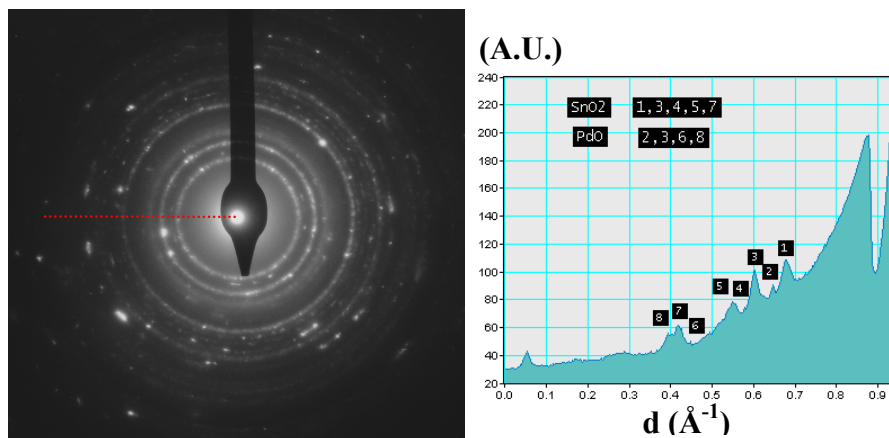


**Figure 5.13.** SAED pattern of sample before reduction with its corresponding profile. Notice that palladium is present as PdO.

clusters, palladium, for high loading samples, can be just found in its oxidized phase. In this way, Ueda et al. [24], in their XRD measurements revealed that Pt exists as metallic state in the Pt catalysts but PdO was observed in the as-grown Pd catalysts. The main part of this work suggest that the formation of PdO occurs during the annealing in air in order to sinter the SnO<sub>2</sub> nanopowders for temperatures similar to that used in our annealings (600 °C) [25, 26, 27]. Egashira et al. [28], verified that Pd oxidation is possible at temperatures as low as 300 °C in presence of oxygen and consequently, at higher temperature (600 °C), PdO is the predominant species and is responsible for the catalytic activity. Nevertheless, all the works we found that described the phenomena used low resolution techniques such as XPS [22, 23, 26], XRD [24], or even SEM [25, 27]. The innovation in our work, will be the atomic description of the phenomena, by using microscopic techniques such as HRTEM, which will allow us to follow the evolution of PdO clusters to Pd when submitting them to a reduction process.

In this way, HRTEM micrographs have helped us to confirm the presence of PdO nanoclusters. As shown in *figure 5.14*, PdO nanoclusters have been found to be placed on SnO<sub>2</sub> nanoparticles surface. However, in

## 5. Metal Ultradispersion

---

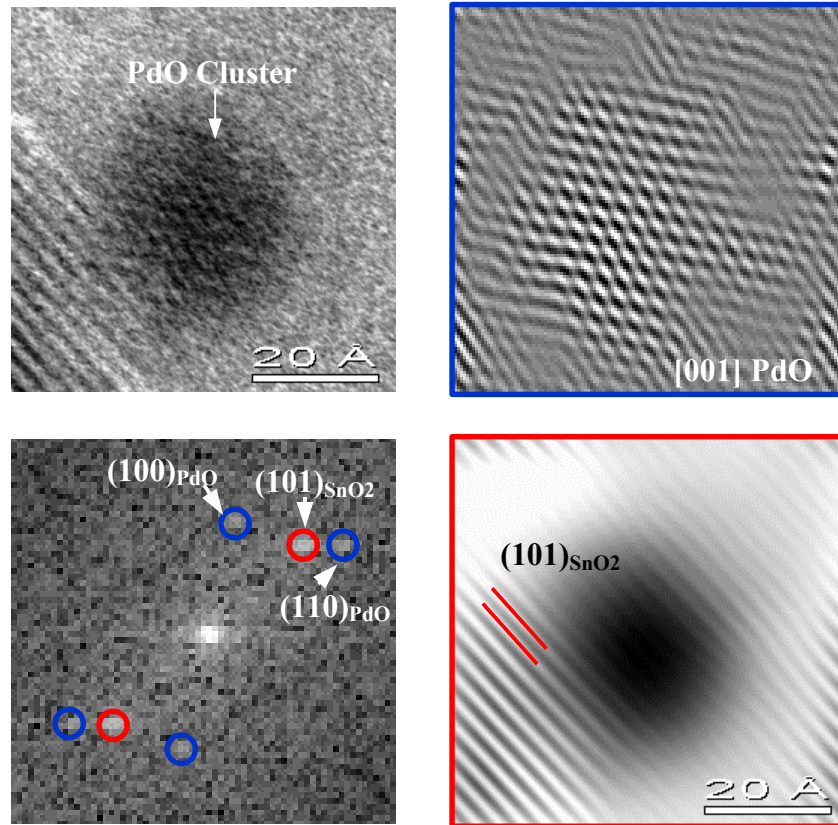


**Figure 5.14.** Spherical PdO nanocluster lying on SnO<sub>2</sub> surface. No epitaxial relationship has been found.

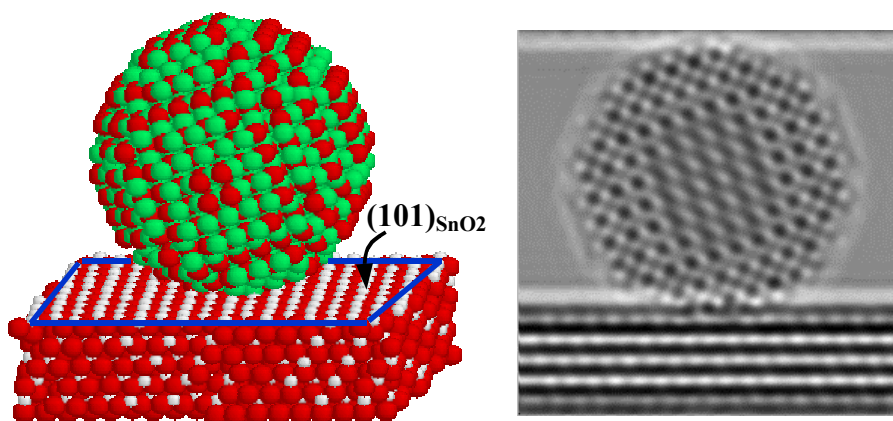


**Figure 5.15.** A Spherical nanocluster model has been tried out for PdO cluster morphology description. Simulation results obtained are in good agreement with the HRTEM experimental images (e.g. *figure 5.14*).

this case, the cluster lies down on the support surface without any evidence of epitaxial growth, since there is no alignment between planes. This result can be extended to the rest of PdO clusters in the as-grown sample, as no evidence of epitaxial growth was observed. We also extracted information from the HRTEM micrograph by isolating the SnO<sub>2</sub> planes from those corresponding to the PdO cluster. DIP has been carried out to determine the possible orientation relationship between cluster and support.

The exact morphology of the PdO nanocluster can not be determined from the image obtained. It has been necessary to appeal to CIS to obtain an estimation of the cluster shape. Several models have been tried out. Nevertheless, the simplest one, the spherical, seems to show the best agreement with the experimental images. In *figure 5.15*, we show the spherical model tested as well as its corresponding CIS. The PdO cluster has been modeled as a sphere just deposited (lying down) on the SnO<sub>2</sub> surface. The (101) SnO<sub>2</sub> plane has been selected to be the support surface. Notice that in order to obtain the experimental desired contrast, the support was tilted 6° with respect to the vertical axis (z), and 10° out of the lateral axis (y). On the other hand, the PdO nanocluster has been built up as a 18 Å diameter sphere imaged in its [001] zone axis. The cluster was also tilted -100° around the zone axis, out of the [100] vertical direction. The CIS image has been obtained in the Scherzer defocus, and has a resolution of 256x256 pixels, and the lateral dimension of the image is 50 Å.

CIS are in good agreement with experimental results. PdO nanoclusters can be considered spherical and moreover without epitaxial growing on semiconductors surface. The observation of several other PdO nanoclusters did not give us new information, as they looked like randomly oriented on supports surface, and all of them adopted quasi-spherical shapes. This is the reason why we won't extend further our analysis on PdO nanoclusters distribution and placement, and we will center our efforts in analyzing the palladium behavior after a reduction process.

### 5.4.2 Sample Nanostructure After Reduction

The sample with 7.06 Pd wt.% has been submitted to an ex-situ reduction process at 200 °C. In *figure 5.16*, we show a general TEM view of the sample grown by the microwave method with high Pd loading after reduction.

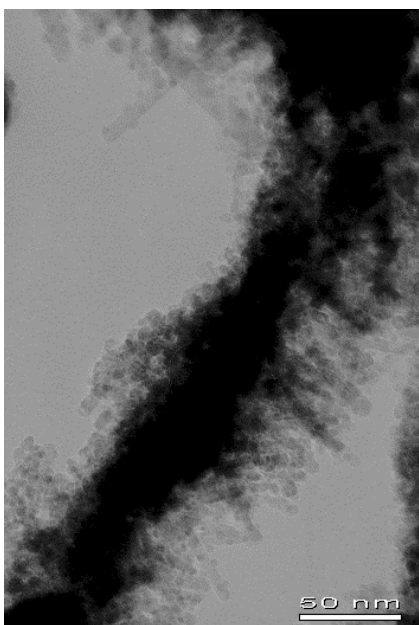


**Figure 5.16.** General TEM view of the sample prepared by the microwave method with high Pd wt.% loading after reduction process.

As it was shown in the former *Section*, some of the SnO<sub>2</sub> nanoparticles adopted stick-like shape before reduction, however, after the reduction treatment the main part of the SnO<sub>2</sub> nanoparticles adopts the stick-like morphology. It looks like the reduction process dramatically enhances the influence of Pd over SnO<sub>2</sub> nanoparticles morphology, leading to a rectangular prism shape faceting.

A magnified detail of these SnO<sub>2</sub> stick-like nanoparticles is shown in *figure 5.17*. It is important to notice that the SnO<sub>2</sub> stretched structures are decorated with dark contrast clusters. A further analysis is needed in order to determine the

cluster nature. In this way, we have analyzed the SAED patterns obtained for the sample after reduction.

In *figure 5.18*, we show the typical SAED pattern obtained for our high palladium loading sample after reduction. A profile analysis has determined the crystalline composition of the sample. In *table 5.6*, we show the correspondence of the rings present in the pattern with the atomic planes and structure.

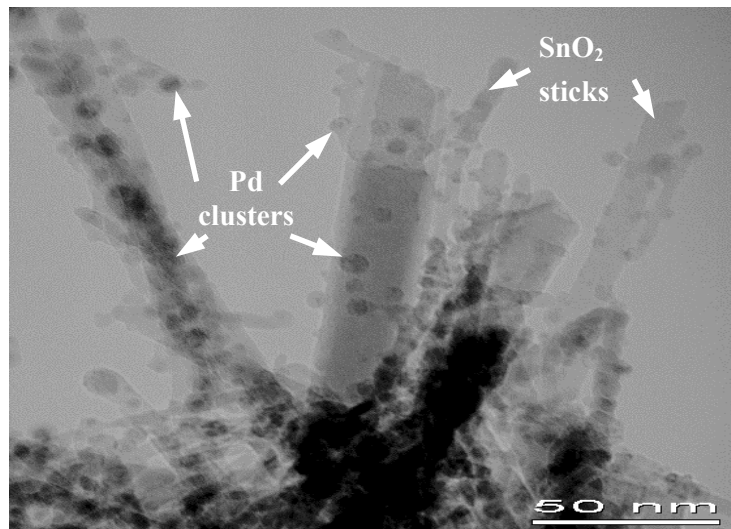


**Figure 5.17.** The main part of SnO<sub>2</sub> nanoparticles adopted rectangular prism shape (stick-like) after reduction.

# Ring	d (Å)	plane	Phase
1	3.35	(110)	SnO <sub>2</sub>
2	2.64	(101)	SnO <sub>2</sub>
3	2.37	(200)	SnO <sub>2</sub>
4	2.31	(111)	SnO <sub>2</sub>
A	2.25	(11-1)	Pd
B	1.95	(200)	Pd
5	1.76	(211)	SnO <sub>2</sub>

**Table 5.6.** SAED pattern profile indexation corresponding to that shown in *figure 5.18*, for sample after reduction process.

An important change has occurred with respect to the pre-treated sample. The absence of the PdO slight rings in the SAED pattern and the presence of metallic palladium corresponding rings, demonstrate the efficiency of the reduction process. After these results we can assume that

## 5. Metal Ultradispersion

the dark contrast clusters decorating the SnO<sub>2</sub> nanoparticles surface are composed of Pd. Nevertheless, a complete analysis of the SnO<sub>2</sub> stick-like particles and the noble metal nanoclusters has been made by means of HRTEM in order to confirm it.

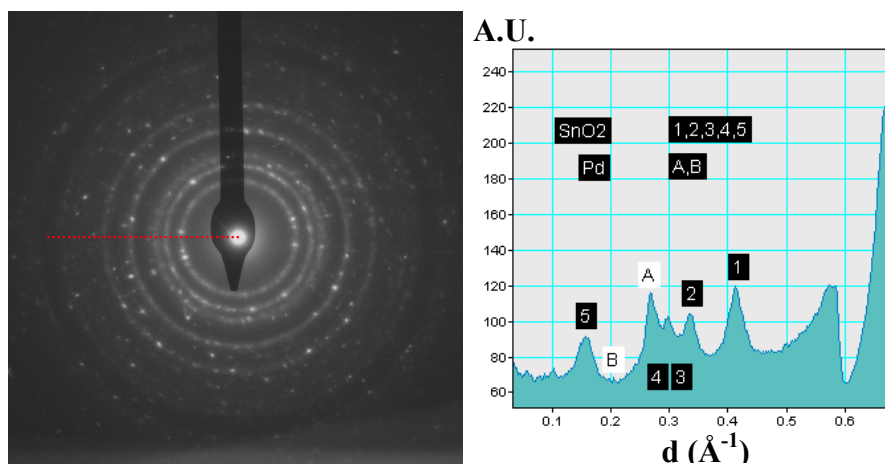


**Figure 5.18.** TED pattern of sample after reduction with its corresponding profile. Notice that palladium is present in its metallic phase.

### 5.4.2.1 Stick-like SnO<sub>2</sub> Nanoparticles Structure

HRTEM micrographs have provided us enough information to build up the stick-like model. In *figure 5.19*, we show a cross-section profile view of a SnO<sub>2</sub> nanostick. This kind of images has helped us to determine the particle contour, or particle faceting planes. A DIP analysis of the image indicates that the top surface corresponds to the (001) plane. From the digital diffraction pattern obtained, we also find that the nanoparticle really adopts rectangular prism morphology, with lateral long faces corresponding to {110} planes. We should point out that these planes, {110}, have been reported to be the thermodynamically most stable in the case of SnO<sub>2</sub> nanostructures [29, 30, 31]. Measures made in several nanosticks, show that they have squared cross-section with typical widths of 5 to 25 nanometers, and lengths up to 1  $\mu$ m. If we take into account the lateral nanostick surfaces, as well as the border facets, we can describe the complete nanostick structure

using a finite number of faceting surface planes. In *table 5.7*, we show the 18 faceting planes used to create the nanostick model shown in *figures 5.19*, *5.20* and *5.21*.

Faceting plane	d (Å)	# planes	Faceting plane	d (Å)	# planes
(110)	3.35	7.00	(-110)	3.35	7.00
(1-10)	3.35	7.00	(-1-10)	3.35	7.00
(001)	3.19	15.00	(00-1)	3.19	15.00
(200)	2.37	13.00	(020)	2.37	13.00
(-200)	2.37	13.00	(0-20)	2.37	13.00
(111)	2.31	21.00	(11-1)	2.31	21.00
(-111)	2.31	21.00	(-11-1)	2.31	21.00
(1-11)	2.31	21.00	(1-1-1)	2.31	21.00
(-1-11)	2.31	21.00	(-1-1-1)	2.31	21.00

**Table 5.7.** Plane faceting using to create the nanostick model.  $D$  is the distance between planes and  $\#$  is referred to the number of plane spacings from the origin where the faceting is applied.

In the example shown in the former *table* the particle created have a squared cross-section with  $46.9 \text{ \AA}$  of width and  $95.7 \text{ nm}$  of length. A cross-section profile view of the model is also shown in *figure 5.19.c*. A CIS of the model proposed has been carried out and showed in *figure 5.19.d*. The simulated image has a resolution of  $256 \times 256$  pixels, and a lateral size of  $60 \times 60 \text{ \AA}$ . Moreover, the image has been obtained under the Scherzer defocus conditions.

In *figure 5.20*, a lateral view of the model described above is shown. The particles found experimentally are longer than the model created, nevertheless, we have built up a shorter model to reduce the computer calculation time. In *figure 5.21*, we show lateral view CIS of the model. The simulations have been obtained for the most common particle orientations experimentally found. All images have a resolution of  $256 \times 256$  pixels and a

## 5. Metal Ultradispersion

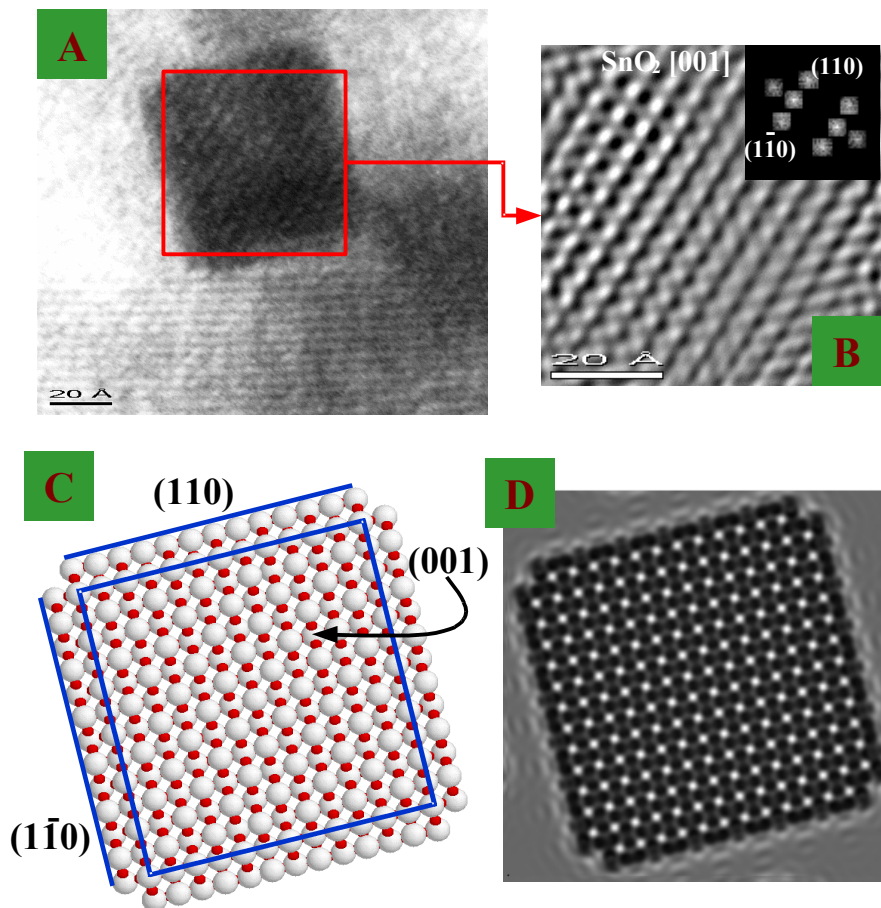


**Figure 5.19.** (A) HRTEM micrograph corresponding to a SnO<sub>2</sub> “stick” visualized in the [001] zone axis. (B) corresponding filtered image. (C) “Stick” model oriented in the [001] direction. (D) CIS of the model in (C), image window size is 60x60 Å and it has been obtained in the Scherzer defocus.

lateral length size of 100 Å. Images have been also simulated in the Scherzer defocus conditions. Notice that the atomic plane contrast changes when tilting the model around the different axes.

The SnO<sub>2</sub> structures experimentally observed are similar to those reported by Pan et al. [32] in a recent work published in *Science*. In their work, they synthesized ultralong belt-like nanostructures (so-called nanobelts) of semiconducting oxides such as tin oxide or indium oxide. Their oxide nanostructures, as well as ours, are pure, structurally uniform,

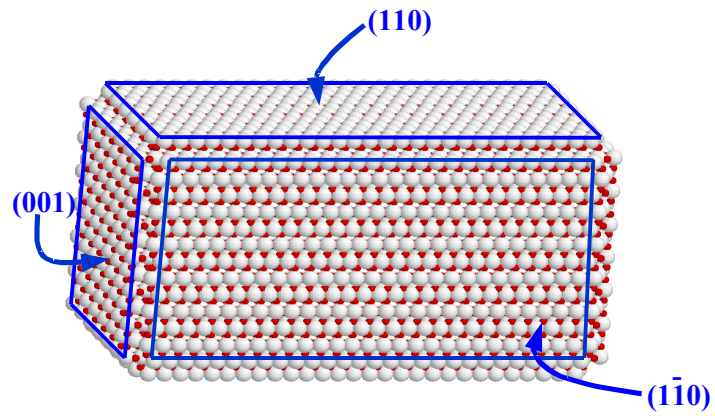


**Figure 5.20.** SnO<sub>2</sub> stick-like nanoparticle model. The model was used in the computer image simulations (CIS) carried out in this *Chapter*.

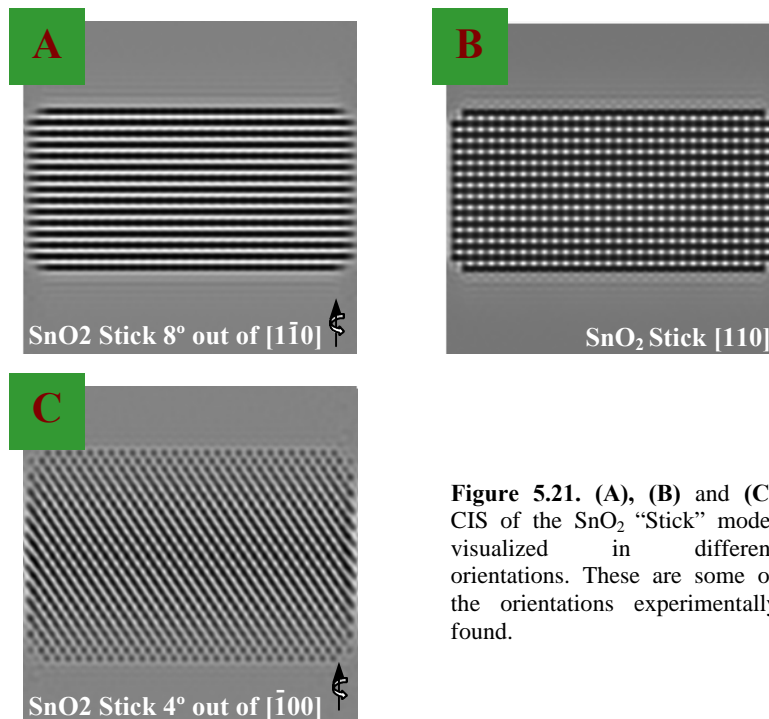


**Figure 5.21.** (A), (B) and (C) CIS of the SnO<sub>2</sub> “Stick” model visualized in different orientations. These are some of the orientations experimentally found.

## 5. Metal Ultradispersion

---

single crystalline and free of defects and dislocations. The main difference between them, is the nanostructure length, since in their case, the nanobelts have lengths up to few millimeters, while ours have lengths just up to 1 micron. Anyway, they suggested that oxide nanobelts could be “doped” with different elements and used for fabricating nanosized sensors. In this work, we show that metal loading is possible in such special structures, and furthermore sensing response obtained with them is satisfactory as we will show at the end of this *Section*.

Once the support particle geometry has been completely determined, in the following we are going to study the noble metal clustering on nanosticks surface.

### 5.4.2.2 Palladium Clusters and Tin Oxide Nanosticks Epitaxy

As shown in *figure 5.22*, after the ex-situ reduction, palladium atoms nucleate in metallic phase nanoclusters epitaxed on {110} SnO<sub>2</sub> stick-like particle surfaces. In the following, we will show a detailed study of the epitaxial relationships found in this sample. The epitaxial planes have been determined from HRTEM profile view images, as that shown in the selected area squared in red in *figure 5.22*. From this selection, we observe that

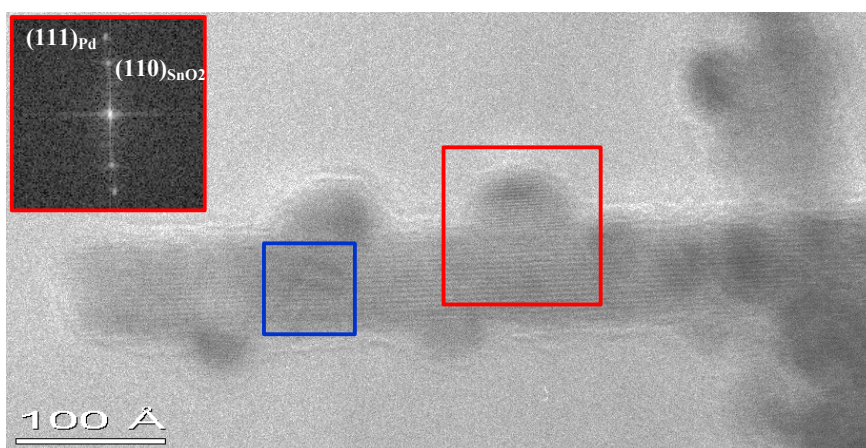


**Figure 5.22.** HRTEM micrograph showing the Pd nanoclusters on a stick-like SnO<sub>2</sub> nanoparticle surface. The digital diffractogram of the squared area contains frequency information about SnO<sub>2</sub> and Pd planes.

$(111)_{\text{Pd}}$  planes are parallel to the  $(110)_{\text{SnO}_2}$ , as it shows the obtained digital diffractogram. In *figure 5.23*, we have magnified the mentioned red selection. Palladium nanocluster  $(111)$  planes can be clearly seen, as well as the parallel  $\text{SnO}_2$   $(110)$  planes. Image filtering has been carried out in order to separate and enhance noble metal and semiconductor oxide phases (on the right side of *figure 5.23*).

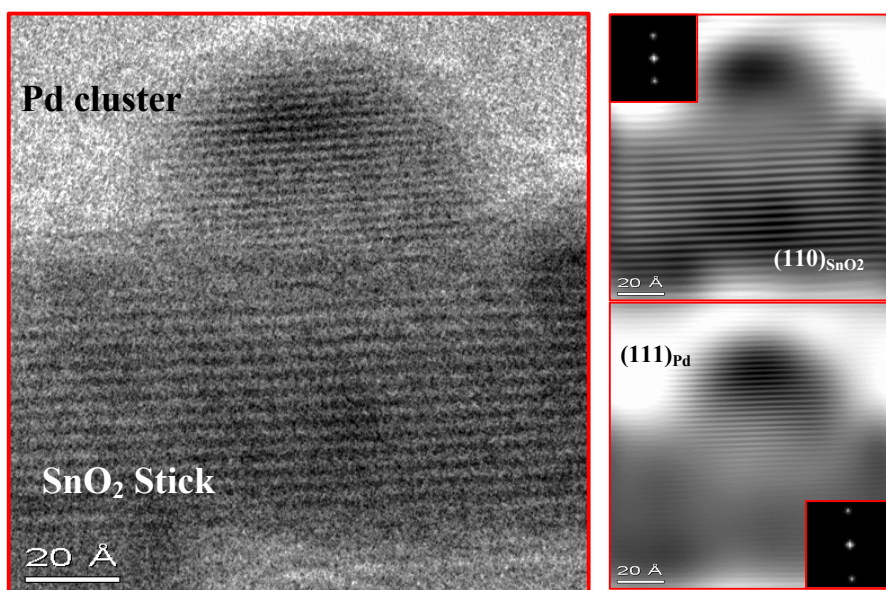


**Figure 5.23.** Magnified detail of the area squared in red in *figure 5.22*. On the right side pictures we show the filtered images where we enhanced Pd and  $\text{SnO}_2$  planes separately by selecting the appropriate spots in the digital diffractogram.

For the interfacial relation obtained from profile view images, we have tried out two possible epitaxial models:  $[1-21](111)_{\text{Pd}} \parallel [001](110)_{\text{SnO}_2}$  (*Model A*) and  $[1-10](111)_{\text{Pd}} \parallel [001](110)_{\text{SnO}_2}$  (*Model B*). Both models are shown in *figures 5.24a* and *5.24b* respectively. On one hand, the first model proposed (*A*) is similar to that suggested by Suzuki and co-workers [33] in the case of palladium epitaxed on  $(110)$   $\text{TiO}_2$  substrates (with similar rutile structure than  $\text{SnO}_2$ ). On the other hand, the second model proposed (*B*) has been created looking for another good fit between palladium and tin oxide

## 5. Metal Ultradispersion

atomic positions, and as we know, this is the first time that this epitaxial relation has been described.

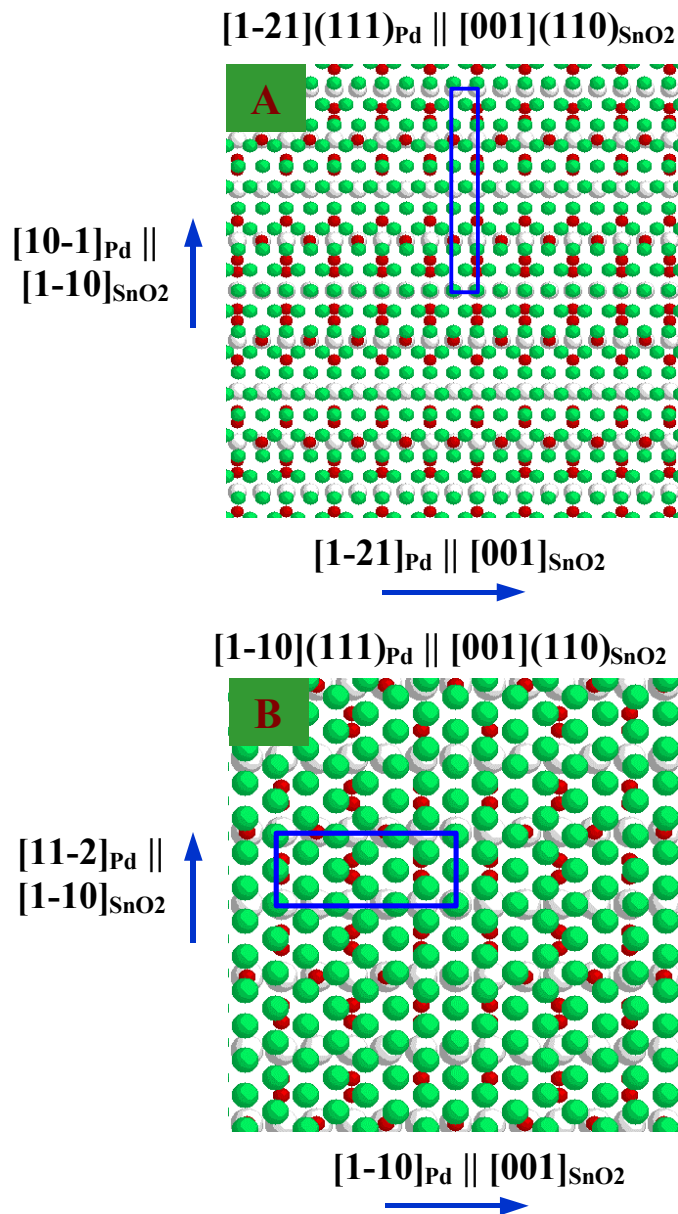


**Figure 5.24.** Epitaxial relationships have been studied after reduction for samples with high Pd loading. The epitaxial models proposed (A and B) after profile view analysis (*figures 5.22 and 5.23*) are shown above.

A plan (top) view of *Model A* is shown in *figure 5.24a*. The atomic radii shown in scheme have been reduced to let us observe the atomic projections in the zone axis. There is a good coincidence between  $(1-21)_{\text{Pd}}$  and  $(002)_{\text{SnO}_2}$  planes. The lateral misfit between them is just  $-0.3\%$ ,  $d(1-21)_{\text{Pd}} = 1.588 \text{ \AA}$  and  $d(002)_{\text{SnO}_2} = 1.593 \text{ \AA}$ . Moreover, if we consider  $(10-1)_{\text{Pd}}$  and  $(1-10)_{\text{SnO}_2}$  planes, we can obtain a new coincidence relation. In this case, every five  $(10-1)_{\text{Pd}}$  plane spacings a platinum atom coincide with a titanium atom in four  $(1-10)_{\text{SnO}_2}$  plane spacings, giving an equivalent misfit of  $2.6\%$ ;  $5 \cdot d(10-1)_{\text{Pd}} = 5 \cdot 2.75 \text{ \AA} = 13.75 \text{ \AA}$ ;  $4 \cdot d(1-10)_{\text{SnO}_2} = 4 \cdot 3.35 \text{ \AA} = 13.40 \text{ \AA}$ , results are summarized in *table 5.8*. This structural correspondence allows us to define a small-size coincidence cell that can be repeated periodically along the  $[1-21]_{\text{Pd}}$  and  $[10-1]_{\text{Pd}}$  directions. The coincidence cell has been marked in *figure 5.24a*, and its dimensions are  $1 \cdot [1-21]_{\text{Pd}} \times 5 \cdot [10-1]_{\text{Pd}}$ . The epitaxial relationship can be described as follows:  $[1-21](111)_{\text{Pd}} \parallel [001](110)_{\text{SnO}_2}$ .

N·Plane 1	N·Plane 2	D1 (Å)	D2 (Å)	misfit (%)
$(1-21)_{\text{Pd}}$	$(002)_{\text{SnO}_2}$	1.588	1.593	-0.3
$5 \cdot (10-1)_{\text{Pd}}$	$4 \cdot (1-10)_{\text{SnO}_2}$	5·2.75	4·3.35	2.6

**Table 5.8.** Epitaxial relations for the model presented in *figure 5.24a*.

In the case of *Model B* (*figure 5.24b*), and taking  $(11-2)_{\text{Pd}}$  and  $(1-10)_{\text{SnO}_2}$  planes as reference in the interface, we obtain the following epitaxial relation: every two  $(11-2)_{\text{Pd}}$  plane spacings, a palladium atom coincides with a Sn atom in a  $(1-10)_{\text{SnO}_2}$  plane. The lateral misfit between them is  $-5.4\%$ ,  $2 \cdot d(11-2)_{\text{Pd}} = 2 \cdot 1.587 \text{ \AA} = 3.174 \text{ \AA}$  and  $d(1-10)_{\text{SnO}_2} = 3.35 \text{ \AA}$ . Moreover, if we consider  $(1-10)_{\text{Pd}}$  and  $(002)_{\text{SnO}_2}$  planes, we can obtain a new coincidence relation. In this case, every three  $(1-10)_{\text{Pd}}$  plane spacings a palladium atom coincide with a tin atom in five  $(002)_{\text{SnO}_2}$  plane spacings, giving an equivalent misfit of  $3.4\%$ ;  $3 \cdot d(1-10)_{\text{Pd}} = 3 \cdot 2.75 \text{ \AA} = 8.25 \text{ \AA}$ ;  $5 \cdot d(002)_{\text{SnO}_2} = 5 \cdot 1.595 \text{ \AA} = 7.975 \text{ \AA}$ , results are summarized in *table 5.9*. Using this structural correspondence we can also define a small-size coincidence cell that is now repeated periodically along the  $[11-2]_{\text{Pd}}$  and  $[1-10]_{\text{Pd}}$  directions. The coincidence cell has been marked in *figure 5.24b*, and its dimensions are

## 5. Metal Ultradispersion

$2 \cdot [11-2]_{\text{Pd}} \times 3 \cdot [1-10]_{\text{Pd}}$ . This epitaxial relationship can be described as follows:  $[1-10](111)_{\text{Pd}} \parallel [001](110)_{\text{SnO}_2}$ .

N·Plane 1	N·Plane 2	D1 (Å)	D2 (Å)	misfit (%)
$2 \cdot (11-2)_{\text{Pd}}$	$(1-10)_{\text{SnO}_2}$	2·1.587	3.35	-5.4
$3 \cdot (1-10)_{\text{Pd}}$	$5 \cdot (002)_{\text{SnO}_2}$	5·1.595	3·2.75	3.4

**Table 5.9.** Epitaxial relations for the model presented in *figure 5.24b*.

Once we have presented the two a priori best possibilities for epitaxial fitting in the  $\{110\}$   $\text{SnO}_2$  surfaces, the next step in our work has been focussed to determine which one of them is the followed by our palladium nanoclusters. By now, we have found the planes placed in the interface by using the HRTEM profile view images. In the following, we

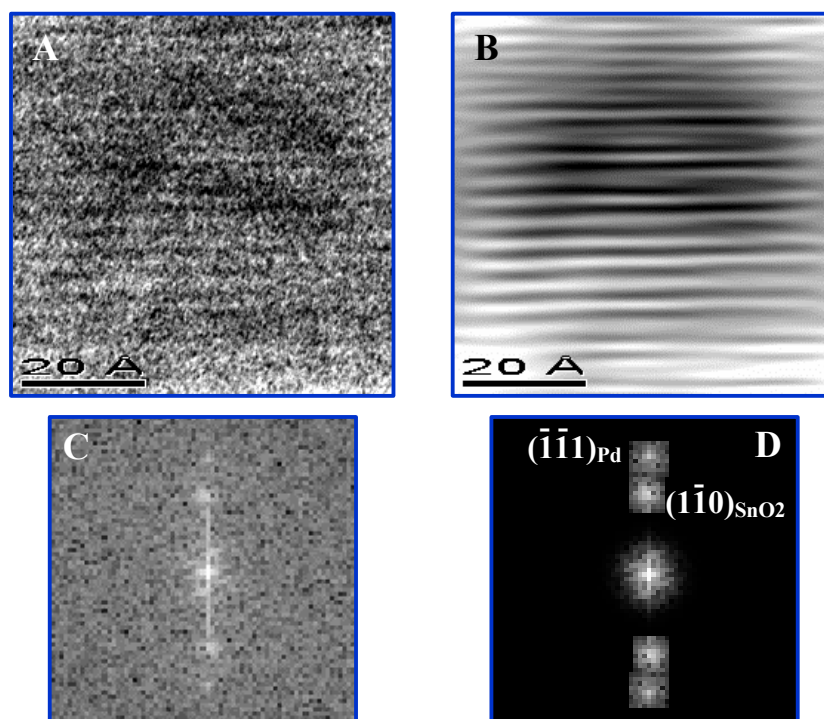


**Figure 5.25.** (A) Plan view magnified HRTEM detail from selection squared in blue in *figure 5.22*. (B) Filtered image showing Moiré fringes due to Pd and  $\text{SnO}_2$  planes constructive interferences. (C) Digital diffractogram of (A). (D) Filtered diffractogram used to obtain (B).

will use the information obtained from the HRTEM plan view images in order to determine the orientation relationship of palladium clusters versus tin oxide support structure in the interface planes. In *figure 5.25a*, we show the magnified detail squared in blue in *figure 5.22*. In this image, we can observe the plan view Moiré fringes created by the constructive interference between SnO<sub>2</sub> and Pd parallel planes. If we can extract the plane spacing information of both planes, we will be able to index the corresponding family planes and obtain the orientation relationship between metal cluster and support on the interface. In this way, we obtained the digital diffractogram of the experimental image (*figure 5.25c*). From the digitized FFT we find that two parallel frequencies (or spots) are parallel. In *figure 5.25d*, we show the filtered spots, and their corresponding indexation. After reciprocal space analysis we find that (-1-11)<sub>Pd</sub> planes are aligned with (1-10)<sub>SnO2</sub> planes. In *figure 5.25b*, we show the filtered image corresponding to Moiré fringes visualized in *figure 5.25a*.

The results obtained above do still not clarify the orientation relationship between cluster and support, as (-1-11)<sub>Pd</sub> planes are not included in (111)<sub>Pd</sub> surface, which is the one placed in the interface. We have to take into account that in a plan view image, we sometimes observe the projection of some planes, which do not need to be included in the plane perpendicular to the zone axis direction imaged. In this way, and in order to obtain the desired orientation relationship, it is necessary to study the stereographic projections of the planes of interest along [111]<sub>Pd</sub> and [110]<sub>SnO2</sub> directions. From the stereographic projections shown in *figure 5.26*, we can easily find that (-1-11)<sub>Pd</sub> plane projection is aligned with (-1-12)<sub>Pd</sub> plane projection and therefore aligned with (1-10)<sub>SnO2</sub> projection. These results indicate that the second epitaxial model suggested above (*Model B*) is in good agreement with the experimental results. The main part of the palladium nanoclusters found in our reduced specimens, seem to follow this epitaxial relationship, therefore, in the following we will assume this relation: [1-10](111)<sub>Pd</sub> || [001](110)<sub>SnO2</sub> or the equivalent [11-2](111)<sub>Pd</sub> || [1-10](110)<sub>SnO2</sub>.

## 5. Metal Ultradispersion

---

At the moment we have obtained the geometrical model of the tin oxide support nanoparticle as well as the epitaxial relationship between noble metal nanocluster and support surface. In the following, we will center our efforts in noble the noble metal nanoclusters morphology analysis.

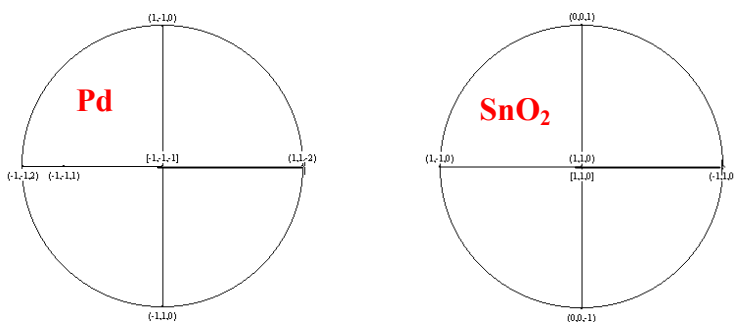


**Figure 5.26.** Stereographic projections describing the orientation relationship obtained in *figure 5.25*. After stereographic analysis we obtain that the epitaxial relationship followed by Pd clusters is that expressed in *figure 5.24.b*.

### 5.4.2.3 Metal Nanoclusters Morphology

In order to determine the palladium nanoclusters morphology, we have built up several cluster-support models, considering the possible geometries.

The metal nanoclusters found have diameter sizes bigger than 3 nm. For such a big sizes, C. Barreteau and co-workers [34], determined that the relative energy stability in palladium clusters, becomes favorable to cuboctahedrons versus icosahedrons. Therefore, the models built have taken into account the cuboctahedral morphology. In the first model (*M1*), we considered a cuboctahedral palladium nanocluster with triangular and square faces (*figure 5.27.M1*). In the second model selected (*M2*), we have tried out with a cuboctahedral nanoparticle with hexagonal and square faces (*figure 5.27.M2*). Models *M1* and *M2* correspond to the two possible cuboctahedral morphologies. Moreover, we have also tried out a spherical model (*M3*), since in the studies made in the case of platinum loaded on titania

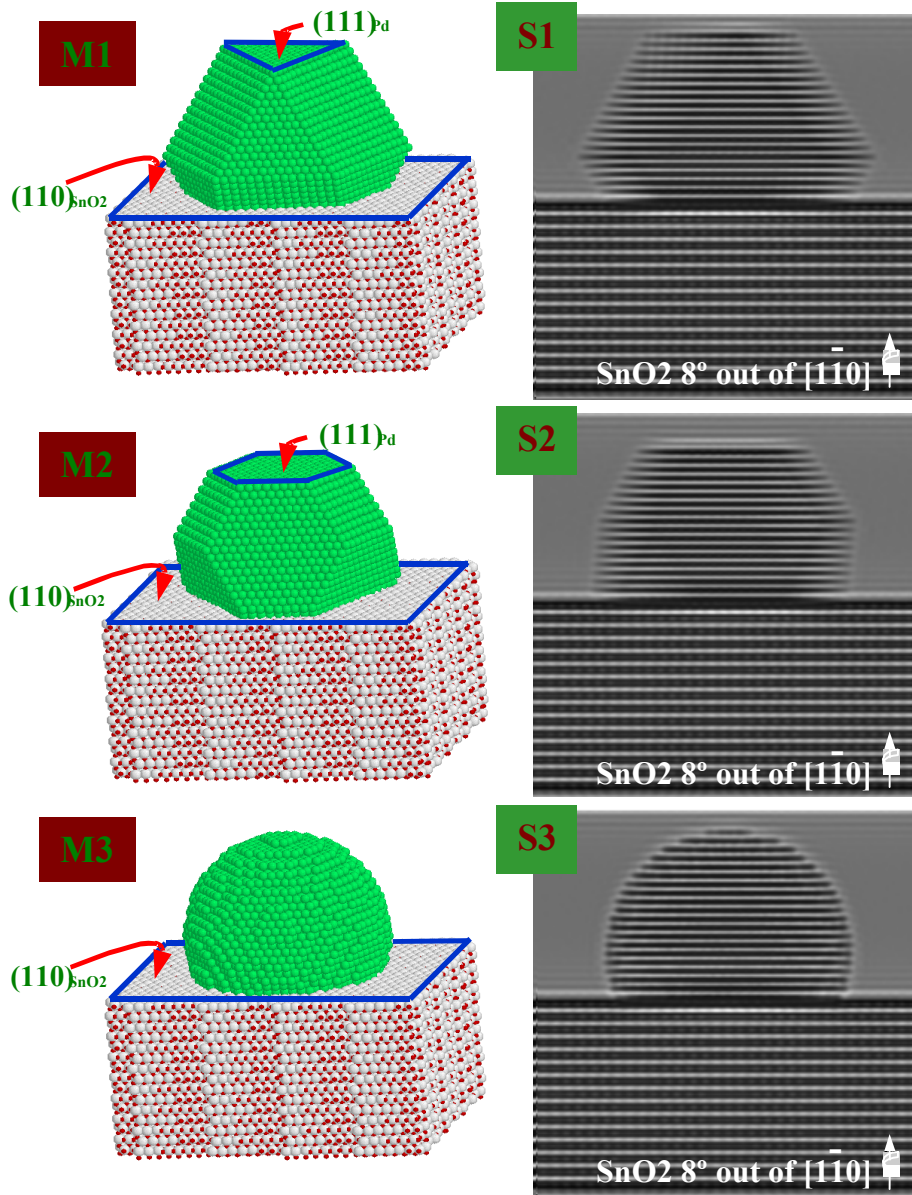


**Figure 5.27.** Several models for cluster morphology have been built up (M1, M2, M3) and simulated (S1, S2, S3). M1: Truncated cuboctahedron with triangular and square faces. M2: Truncated cuboctahedron with hexagonal and square faces. M3: Truncated sphere.

## 5. Metal Ultradispersion

---

nanopowders (*Chapter 4*), we have found that noble metal nanoparticles can also adopt quasi-spherical morphology for diameter sizes  $> 3$  nm.

We want to point out that the three models shown in *figure 5.27* have been built up following the epitaxial relationships found above (*Model B*), where  $[1-10](111)_{\text{Pd}} \parallel [001](110)_{\text{SnO}_2}$  and  $[11-2](111)_{\text{Pd}} \parallel [1-10](110)_{\text{SnO}_2}$ . Notice also that the built clusters have been truncated on their basis, in order to allow a better adaptation with nanosticks support. Clusters sizes taken in the models have been chosen to fit with the palladium nanocluster shown in *figure 5.23*. In this way, for cuboctahedral clusters we used the faceting shown in *tables 5.10* and *5.11*, model *M1* and *M2* respectively. In the case of the spherical model (*M3*) we just selected a 32 Å radius sphere.

In *figures 5.27.S1*, *5.27.S2* and *5.27.S3* we can appreciate the CIS corresponding to models *M1*, *M2* and *M3* respectively. Images have a resolution of 256x256 pixels and a lateral size of 100 Å. All of them have been obtained in the Scherzer defocus conditions, and model was tilted 8 ° out of the [1-10] zone axis in order to exactly reproduce the experimental image. By comparing *figure 5.23* with CIS results, we find that the model that suits better to the experimental results is the one considering a spherical nanocluster (*M3*).

Faceting plane	d (Å)	# planes	Faceting plane	d (Å)	# planes
(111)	2.25	14.00	(11-1)	2.25	14.00
(-111)	2.25	14.00	(-11-1)	2.25	14.00
(1-11)	2.25	14.00	(1-1-1)	2.25	14.00
(-1-11)	2.25	14.00	(-1-1-1)	2.25	14.00
(200)	1.95	14.00	(-200)	1.95	14.00
(020)	1.95	14.00	(0-20)	1.95	14.00
(002)	1.95	14.00	(00-2)	1.95	14.00

**Table 5.10.** Plane faceting using to create the cuboctahedral nanocluster with square and triangular faces (*M1*). *d* is the distance between planes and # is referred to the number of plane spacings from the center where the faceting is applied.

Faceting plane	d (Å)	# planes	Faceting plane	d (Å)	# planes
(111)	2.25	12.00	(11-1)	2.25	12.00
(-111)	2.25	12.00	(-11-1)	2.25	12.00
(1-11)	2.25	12.00	(1-1-1)	2.25	12.00
(-1-11)	2.25	12.00	(-1-1-1)	2.25	12.00
(200)	1.95	16.00	(-200)	1.95	16.00
(020)	1.95	16.00	(0-20)	1.95	16.00
(002)	1.95	16.00	(00-2)	1.95	16.00

**Table 5.11.** Plane faceting using to create the cuboctahedral nanocluster with square and hexagonal faces ( $M2$ ).  $d$  is the distance between planes and # is referred to the number of plane spacings from the center where the faceting is applied.

Once obtained the epitaxial relationships and nanosticks and clusters morphology, we are able to build up a complex model of a whole nanostick decorated with palladium nanocluster in their lateral and top surfaces. This model corresponds to the one shown in *figure 5.28*, where two truncated spherical Pd clusters have been epitaxed to a nanostick portion, reproducing the real palladium disposition observed in the specimens studied. Palladium clusters modeled have equivalent radius sizes corresponding to 21 and 32 Å, for the lateral and top cluster, respectively. The sizes selected tried to agree with those measured in the experimental micrograph shown in *figure 5.22*, where the lateral palladium cluster corresponds to that squared in blue and the top palladium cluster would reproduce the characteristics of that selected in red.

CIS carried out from the complex model described above (also in *figure 5.28*), is in perfect agreement with the experimental image in *figure 5.22*. Notice that we can even observe the Moiré fringes for the lateral palladium nanocluster.

According to the simulated models and the detailed studies made above, Pd nanoclusters adopt spherical morphology and grow epitaxed on SnO<sub>2</sub> stick-like particles after the ex-situ reduction process. Epitaxial growth

## 5. Metal Ultradispersion

---

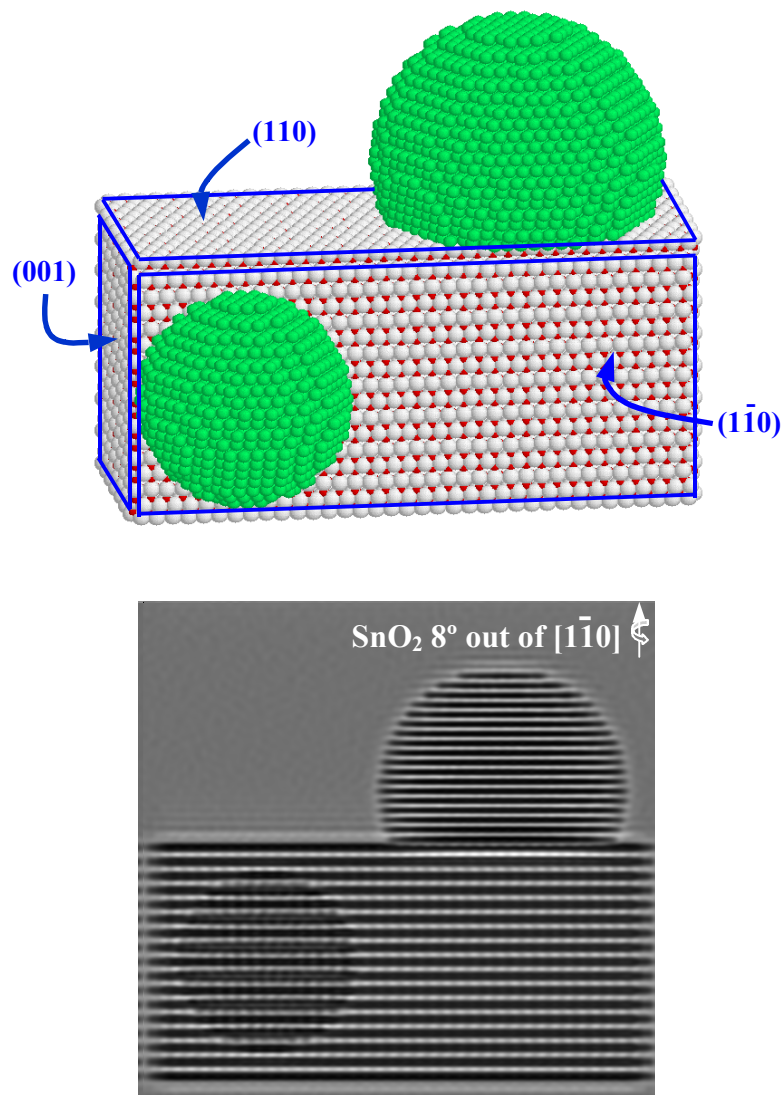


**Figure 5.28.** Complex model for plan and profile view spherical Pd nanoclusters on a stick-like SnO<sub>2</sub> nanoparticle. Epitaxial relationships are in agreement with the ones found experimentally. We also show the simulated model that is in the same orientation conditions as the experimental micrograph shown in *figure 5.22*.

can improve the electrical exchange between metal clusters and semiconductor support, giving a better conducting response in our sensor devices in an environment of reducing gases [10, 35]. In this way, in the next *Section*, we will relate the morphological and structural changes occurred to our specimens with the electrical sensing response obtained in the SGS devices implemented with our material.

### 5.4.3 Structural influence on the Electrical Sensing Response

In the previous *Sections* we have shown the morphological and structural changes that occur in palladium nanoclusters when submitting the sample to a reducing environment. In order to observe the electronic behavior of this materials, we implemented SGS devices as those described in *Chapter 1 (figure 1.1)*, [9]. Afterwards, we submitted the sensor device to flowing gas pulses of synthetic air (SA)/CO, and SA/CH<sub>4</sub>. The experience was carried out in a test chamber [36], and measurements were made at two different heating temperatures (250 and 350 °C).

In *figure 5.29*, we show the sensor response in front of SA/CO and SA/CH<sub>4</sub> gas pulses for 250 °C (*top figure*) and 350 °C (*bottom figure*). When working at the lowest temperature (250 °C), we notice a dramatic reduction of sensor device resistance with the CO and CH<sub>4</sub> exposure. Notice that our device is more sensible to the presence of CO than to CH<sub>4</sub>, as fewer CO ppm can induce greater conductance changes. As CO and CH<sub>4</sub> have been reported to act in a similar reducing way as H<sub>2</sub> [37], we expect that the structural changes observed for reduction treatments under H<sub>2</sub> atmosphere must be similar to those occurred under CO and CH<sub>4</sub>. In this way, we suggest that the presence of palladium oxide non-epitaxed or palladium epitaxed clusters is responsible of the changes in the conduction behavior of the sensing material.

In previous works, we had already reported that the changes in the charge state of palladium clusters, induces a variation of the surface barrier

## 5. Metal Ultradispersion

height and therefore leads to a conductance change on the base oxide [35, 38, 39]. In this case, the base semiconductor has a transducer role of the changes induced in the additive particles by their interaction with the gas. This changes could be visualized in-situ using STM maps during reducing

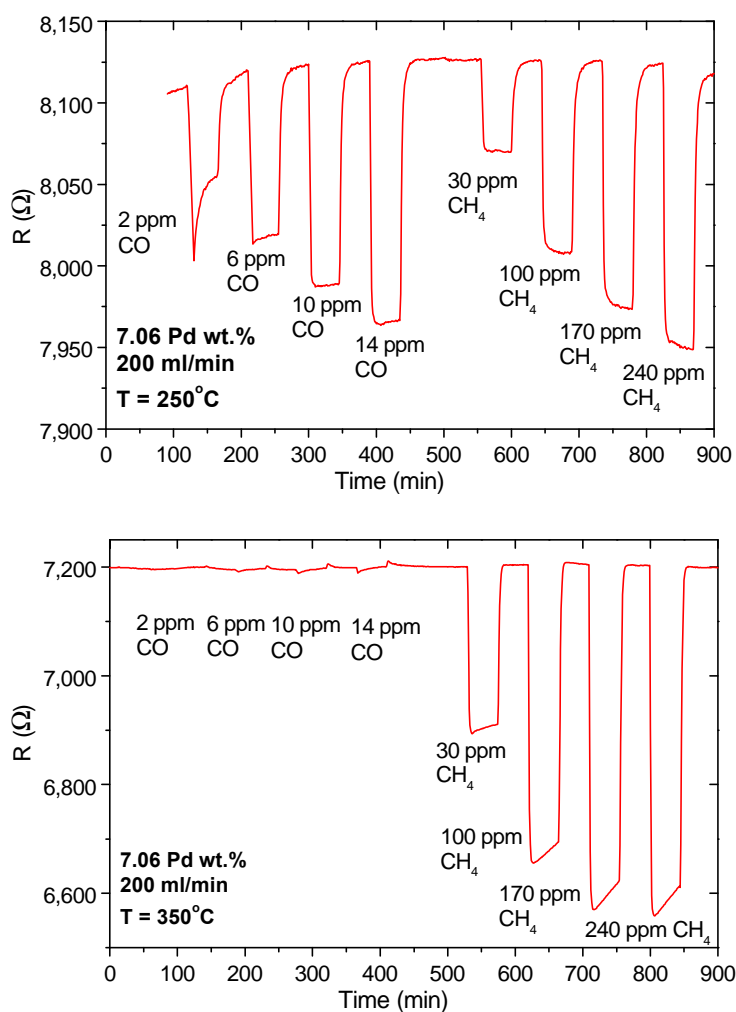


**Figure 5.29.** Sensing response of the 7.06 Pd wt.% sample prepared by the microwave method at 250 and 350 °C, respectively. Response was measured under CO and CH<sub>4</sub> gas pulses, which induces material reduction. Notice that reduction/oxidation processes are reversible when introducing again synthetic air. At higher temperatures (350 °C), the important decrease of sensor sensitivity versus CO can be due to the well-known SMSI effect.

gas exposure, as we reported elsewhere [40, 41, 42]. Moreover, several works have been devoted to find the physical explanations to this sensing phenomenon. In this way, in early 90s, Yamazoe et al. [43, 44], introduced the electronic sensitization mechanism in which palladium nanoclusters could modify the work function of the support depending on their oxidation state. Furthermore, Madhusudhana et al. [45], suggested that Pd in the oxygen phase acts as an electron acceptor and traps the charge from SnO<sub>2</sub> conduction band. This trapped charge induces stronger depletion of electrons from the SnO<sub>2</sub> surface causing a rise in resistance. Since the depletion of carriers is related to the density of trapped charge at the surface, Pd clusters having a minimum size of a few nanometers are necessary to affect the resistance. In addition, under the reducing gas ambient, they suggested that reduction and oxidation of Pd continues causing detrapping and trapping electrons. In recent works, Labeau and co-workers [46, 47, 48], in their studies about Pd-Pt/SnO<sub>2</sub> gas sensors have proposed that the reduction of the noble metal aggregates results in an important electron injection into the SnO<sub>2</sub> grain conduction band. This would lead to an increase of the free electron density on the surface and ultimately to a sharp increase of conductance.

After the HRTEM experimental results obtained, we suggest that the increase of conductance proposed by Labeau et al., could be related to the presence of epitaxed palladium nanoclusters on SnO<sub>2</sub> nanoparticles surface. In this way, we suggest that the electron injection is dramatically favored when there exists a good contact between metal nanocluster and oxide surface, and moreover when there is an epitaxial growth, where atomic positions are not randomly distributed and the atom-to-atom charge exchange can be enhanced. On the other hand, the presence of spherical palladium oxide nanoclusters non-epitaxed to semiconductors surface would be responsible of the increasing in the semiconductors working function, as the oxidized nanoclusters would act as electron acceptors trapping the charge and decreasing the conductance, as shown experimentally (*figure 5.29*).

## 5. Metal Ultradispersion

---

As seen above, several works have been devoted to understand the physical mechanisms that rule the gas sensing behavior of Pd/SnO<sub>2</sub> systems. Nevertheless, to our knowledge, it is the first time that an accurate microscopic analysis has been carried out. Our results are in good agreement with the mechanisms exposed above and we think that results exposed in this work should be taken seriously into account for the future comprehension of the sensing phenomena.

On the other hand, when working at higher sensing temperatures (350 °C) we observe an important decrease of the sensor sensitivity versus CO. As it has been widely reported in literature, group VIII noble metals when loaded to TiO<sub>2</sub> semiconductor supports, lost its chemisorption properties after annealing at high temperatures (over 300 °C) in a reduction atmosphere [49, 50, 51, 52, 53]. This change in the catalytic properties has been attributed to the SMSI effect [33, 54]. There have been a great number of studies concerning the metal/metal oxide system since discovery of strong metal support interaction (SMSI) effect in catalytic properties by Tauster et al. [55]. The encapsulation of the metal clusters by oxide species migrated from support is the main mechanism that has been proposed to explain the catalytic property change induced by SMSI. Recently, some evidential reports have appeared in the Pt/TiO<sub>2</sub> system that supported the encapsulation model as a major effect in SMSI. Petsy et al. found that Pt growing in the three dimensional Volmer-Weber mode on the TiO<sub>2</sub> surface at room temperature (RT) was encapsulated by the TiO<sub>x</sub> species after annealing at temperatures above 450 K in ultra-high vacuum (UHV) [56]. The microscopic mechanism of the encapsulation is not clear, although many efforts have been devoted to this subject. Baker et al. [57] found the crystalline Ti<sub>4</sub>O<sub>7</sub> reduced phase to be formed on the Pt clusters after reduction. Whereas Dayte et al. [58], in the Rh/TiO<sub>2</sub> system, reported that amorphous TiO<sub>x</sub> overlayers encapsulated the Rh nanoclusters. These results were also extended by Chang et al. [59] to other metal species as Pt and Pd on TiO<sub>2</sub>. And on the other hand, Haller et al. [60], suggested that the migration of reduced species from the support is accompanied by the

formation of metal-Ti bonds, which provide the thermodynamic driving force for the migration. Encapsulation occurs with  $\text{TiO}_2$  for materials that show a low tendency towards wetting, such as Fe, Pd or Pt, and is not observed for more reactive elements, such as Cr or Hf [61].

The SMSI effect it is reversible since upon reoxidation, the metal particles would recover their original hemispherical shapes losing the metal oxide overlays [62]. Other works also showed how the morphology of Pt clusters on titania could be changed reversibly by alternating oxidation and reduction treatments at high temperature (600 °C) [63].

Although we have been working with  $\text{SnO}_2$  instead of  $\text{TiO}_2$ , we suggest that a similar effect could contribute to the important decrease of the sensing response at high temperatures (350°C) under CO atmosphere. Nevertheless, no encapsulation was observed in our clusters when observed with HRTEM after the ex-situ reduction processes. We want to point out, that our ex-situ treatments were carried out at 200 °C, and that a such low reducing temperature the SMSI effect is not expected to occur, as shown by the good conductance results obtained in our electrical tests (*figure 5.29*). By now, and after our in-situ experiences, we could observe that  $\text{SnO}_2$  is highly reactive to reducing environments, even more than  $\text{TiO}_2$ , in this way, we would also expect that at such a high temperatures (around 300-350 °C) the reduced species could migrate over palladium clusters and produce the SMSI effect. Anyway, further analysis should be made at quite higher temperature treatments (around 300-350 °C), in order to determine if the SMSI effect also occurs in Pd/ $\text{SnO}_2$  systems and that encapsulation of palladium nanoclusters is produced.

## 5.5 Conclusions

In this *Chapter* we have focussed our efforts in studying the catalytic metal ultradispersion as another of the possible catalytic distribution ways. Pd/SnO<sub>2</sub> systems have been analyzed by HRTEM, following the evolution of palladium atoms from monoatomic ultradispersion, in the case of low palladium loadings, to metal clustering, for high palladium loadings.

In the case of low palladium loadings (samples prepared by the electroless method), the as-grown SGS nanopowders present pure tin oxide structure with rounded shapes and a wide size range, from 30 to 300 nm in diameter. HRTEM micrographs show the presence of few PdO nanoclusters on semiconductor particles surface, but not as much as we could expect by comparing with similar loading values in the Pt/TiO<sub>2</sub> samples analyzed in *Chapter 4*.

ICP results suggest that the main part of the Pd atoms does not nucleate in surface nanoclusters, obtaining that these palladium atoms could be placed in an atomic-like ultradispersion on SnO<sub>2</sub>. The small PdO peak obtained by XRD it has been attributed to the palladium forming surface aggregates or clusters, as the atomically ultradispersed palladium can not be detected using this technique.

In-situ and ex-situ reduction experiences have been used in order to visualize ultradispersed atoms, as these treatments provide the palladium atoms with energy enough to nucleate (sinter) in small nanoclusters.

After the reduction treatments, TEM micrographs show that small hills decor the SnO<sub>2</sub> nanoparticles surface. After a detailed HRTEM study we found that the basis of the hills are composed by tin monoxide (SnO) while small palladium nanoclusters are embedded on the top of these hills. As the density of these Pd clusters is far higher than that found before

reduction, we suggest that the main part of this nanoclusters are the result of ultradispersed palladium atoms nucleation (sintering) due to the reduction process.

The in-situ reduction experience have allowed us to observe the reduced hills formation and metal sintering in real-time. The energy transferred by the electrons to the material promotes the breakage of Sn-O bonds, what leads the SnO<sub>2</sub> crystallites to evaporate slowly during irradiation. Tin oxide particle size decrease takes place as a consequence of this process, as well as the growth of hills on nanoparticle surface and metal sintering on the top of this hills.

In the case of high palladium loadings (obtained by the microwave method), we have found that the excess of palladium can influence the SnO<sub>2</sub> growing, determining the faceting of the rutile nanoparticles and modeling the SnO<sub>2</sub> stick-like nanoparticles observed.

In the as-grown sample the main part of Pd atoms nucleate forming small nanoclusters in their oxidized phase (PdO). The typical PdO cluster has been modeled as a sphere just deposited (lying down) on the SnO<sub>2</sub> surface, without epitaxial growing on semiconductors surface.

After the ex-situ reduction treatments, the main part of the SnO<sub>2</sub> nanoparticles adopts the stick-like morphology and a high density of Pd nanoclusters decor their {110} surfaces. Pd nanoclusters have been found to grow epitaxed to the SnO<sub>2</sub> {110} surfaces, following the next epitaxial relationship:  $[1-10](111)_{\text{Pd}} \parallel [001](110)_{\text{SnO}_2}$ . The morphology adopted by this nanoclusters is the spherical, truncated in its (111) basis plane.

We also measured the electrical sensing response of a sensor device implemented with the higher palladium loaded sample. Response was measured under reducing gas flowing pulses (CO and CH<sub>4</sub>) obtaining high sensitivity results.

We have found that the increase of SGS conductance, when working at 250 °C, could be due to an increase in electron injection favored by the

## 5. Metal Ultradispersion

---

good contact and epitaxy between reduced metal nanoclusters and semiconductor oxide surface. On the other hand, the presence of spherical palladium oxide nanoclusters non-epitaxed to semiconductors surface would be responsible of the increasing in the semiconductors working function, as the oxidized nanoclusters would act as electron acceptors trapping the charge and decreasing the conductance.

Nevertheless, at higher temperatures (350 °C), we observe an important decrease of sensor sensitivity versus CO. We suggest that this phenomena can be due to the SMSI effect between metal cluster and oxide support. In this way, further analysis will be carried out in the future in order to determine if palladium metal clusters can be encapsulated by oxide support species as happens in noble metal/TiO<sub>2</sub> systems.

## References

1. M. H. Madhusudhana Reddy and A. N. Chandorkar, E-Beam deposited SnO<sub>2</sub>, Pt-SnO<sub>2</sub> and Pd-SnO<sub>2</sub> thin films for LPG detection, *Thin Solid Films*, **349**, 260-265 (1999).
2. R. Cavicchi, V. Sukharev and S. Semancik, Time-dependent conductance of Pd-doped SnO<sub>2</sub>(110), *Surface Science*, **418**, L81-L88 (1998).
3. J. Arbiol, R. Díaz, A. Cirera, F. Peiró, A. Cornet, J. R. Morante, F. Sanz, C. Mira, J. J. Delgado, G. Blanco and J. J. Calvino, Effects of in-situ and ex-situ reduction of Pd/SnO<sub>2</sub> studied by HRTEM, to be published in *Inst. Phys. Conf. Ser.*
4. C.- B. Lim., S. Oh, Microstructure Evolution and Gas Sensitivities of Pd-Doped SnO<sub>2</sub>-Based Sensor Prepared by 3 Different Catalyst-Addition Processes, *Sensors and Actuators B*, **30**, 223-231 (1996).
5. R. Díaz R, J. Arbiol, A. Cirera, F. Sanz, F. Peiró, A. Cornet and J. R. Morante, Electroless Addition of Catalytic Pd to SnO<sub>2</sub> Nanopowders, submitted to *Chemical Materials*.
6. A. Brenner and G. E. Riddell, *J. Res. Natl. Bur. Stan.*, **37**, 31 (1946).
7. F. A. Lowenheim, *Modern Electroplating*; John Wiley & Sons Inc.: New York, (1974).
8. A. Li, G. Xiong, J. Gu, L. J. Zheng, *Journal of Membrane Science*, **110**, 257 (1996).
9. A. Cirera, New technologies and their characterization for nanostructured SnO<sub>2</sub> gas sensor devices, *PhD. Thesis*, Universitat de Barcelona, Barcelona (2000).
10. A. Cirera, A. Vilà, A. Diéguez, A. Cabot, A. Cornet and J. R. Morante, Microwave processing for the low cost, mass production of undoped and in situ catalytic doped nanosized SnO<sub>2</sub> gas sensor powders, *Sensors and Actuators B*, **64**, 65-69 (2000).
11. A. Diéguez, A. Romano-Rodríguez, J.R. Morante, U. Weimar, M. Schweizer-Berberich and W. Göpel, Morphological analysis of nanocrystalline SnO<sub>2</sub> for gas sensor applications, *Sensors and Actuators B*, **31**, 1-8 (1996).

## 5. Metal Ultradispersion

---

12. S. Bernal, F. J. Botana, J. J. Calvino, C. López, J. A. Pérez-Omil and J. M. Rodríguez-Izquierdo, High-resolution electron microscopy investigation of metal-support interactions in Rh/TiO<sub>2</sub>, *Journal of the Chemical Society, Faraday Trans.*, **92 (15)**, 2799-2809 (1996).
13. K. Suzuki, M. Ichiara and S. Takeuchi, High-resolution electron microscopy of lattice defects in TiO<sub>2</sub> and SnO<sub>2</sub>, *Philosophical Magazine A*, **63**, 657-665 (1991).
14. *JCPDS* 41-1445 (1997).
15. S. Matsushima, K. Kobayashi and M. Kohyama, Semiempirical Band Calculation of Pd-Adsorbed SnO<sub>2</sub> Surface, *Japanese Journal of Applied Physics*, **38**, 4993-4996 (1999).
16. M. L. Cubeiro and J. L. G. Fierro, Selective Production of Hydrogen by Partial Oxidation of Methanol over ZnO-Supported Palladium Catalyst, *Journal Of Catalysis*, **179 (1)**, 150-162 (1998).
17. D. Lomot, W. Juszczyk, Z. Karpinski and F. Bozonverduraz, Evolution and Catalytic Activity of Pd/Gamma-Al<sub>2</sub>O<sub>3</sub> Catalysts Prepared from Chlorine-Free Compounds, *New Journal Of Chemistry*, **21 (9)**, 977-984 (1997).
18. A. Mastalir, F. Notheisz, M. Bartok, T. Haraszti, Z. Kiraly and I. Dekany, Transformation of Carbon-Compounds on Graphimet Catalysts .9. Structural-Properties and Catalytic Activity of Pd-Graphimet, *Applied Catalysis A-General*, **144 (1-2)**, 237-248 (1996).
19. A. Cirera, A. Cabot, A. Cornet, J. R. Morante, CO-CH<sub>4</sub> selectivity enhancement by in-situ Pd-catalyzed microwave SnO<sub>2</sub> nanoparticles for gas detectors using active filter, to be published in *Sensors and Actuators B*.
20. C. P. Udawatte, M. Kakihana and M. Yoshimura, Preparation of pure perovskite-type BaSnO<sub>3</sub> powders by the polymerized complex method at reduced temperature, *Solid State Ionics*, **108**, 23-30 (1998).
21. Y. Zhu, L. Zhang, W. Yao and L. Cao, The chemical states and properties of doped TiO<sub>2</sub> film photocatalyst prepared using the Sol-Gel method with TiCl<sub>4</sub> as a precursor, *Applied Surface Science*, **158**, 32-37 (2000).
22. A. R. Phani, S. Manorama and V. J. Rao, The nature of surface behavior of tin oxide doped sensors: X-ray photoelectron spectroscopy studies before and after exposure to liquid petroleum gas, *Journal of Physics and Chemistry of Solids*, **61**, 985-993 (2000).

23. R. Rella, P. Siciliano, S. Capone, M. Epifani, L. Vasanelli and A. Licciuli, Air quality monitoring by means of sol-gel integrated tin oxide thin films, *Sensors and Actuators B*, **58**, 283-288 (1999).
24. A. Ueda, T. Nakao, M. Azuma and T. Kobayashi, Two conversion maxima at 373 and 573 K in the reduction of nitrogen monoxide with hydrogen over Pd/TiO<sub>2</sub> catalyst, *Catalysis Today*, **45**, 135-138 (1998).
25. G. Tournier, C. Pijolat, R. Lalauze and B. Patissier, Selective detection of CO and CH<sub>4</sub> with gas sensors using SnO<sub>2</sub> doped with palladium. *Sensors and Actuators B*, **26-27**, 24-28 (1995).
26. G. De, A. Licciulli, C. Massaro, A. Quirini, R. Rella, P. Siciliano and L. Vasanelli, Sol-gel derived pure and palladium activated tin oxide films for gas-sensing applications, *Sensors and Actuators B*, **55**, 134-139 (1999).
27. M. Labeau, B. Gautheron, G. Delabouglise, J. Peña, V. Ragel, A. Varela, J. Román, J. Martinez, J. M. González-Calbet and M. Vallet-Regi, Synthesis, structure and gas sensitivity properties of pure and doped SnO<sub>2</sub>. *Sensors and Actuators B*, **15-16**, 379-383 (1993).
28. M. Egashira, M. Nanashima, and S. Kawsumi, *ACS Symposium Series, American Chemical Society, Washington, DC*, **309**, 71-82 (1986).
29. B. Theil, R. Heilbig, Growth of SnO<sub>2</sub> single crystals by a vapor phase reaction method, *Journal of Crystal Growth*, **32**, 259-264 (1976).
30. S. Semancik, F. B. Fryberger, Model studies of SnO<sub>2</sub> based gas sensors: vacancyeffects and Pd additive effects, *Sensors and Actuators B*, **1**, 97-102 (1990).
31. J. Goniakowski, M. J. Gillan, The adsorption of H<sub>2</sub>O on TiO<sub>2</sub> and SnO<sub>2</sub> (110) studied by first-principles calculations, *Surface Science*, **350**, 145-158 (1996).
32. Z. W. Pan, Z. R. Dai and Z. L. Wang, Nanobelts of Semiconducting Oxides, *Science*, **291**, 1947-1949 (2001).
33. T. Suzuki and R. Souda, The encapsulation of Pd by the supporting TiO<sub>2</sub> (110) surface induced by strong metal-support interactions, *Surface Science*, **448**, 33-39 (2000).
34. C. Barreteau, M. C. Desjonquères and D. Spanjaard, Theoretical study of the icosahedral to cuboctahedral structural transitions in Rh and Pd clusters, *The European Physical Journal D*, **11**, 395-402 (2000).
35. A. Cabot, J. Arbiol, J. R. Morante, U. Weimar, N. Bârsan and W. Göpel, Analysis of the noble metal catalytic additives introduced by impregnation of as

## 5. Metal Ultradispersion

---

obtained SnO<sub>2</sub> sol-gel nanocrystals for gas sensors, *Sensors and Actuators B*, **70**, 87-100 (2000).

36. A. Cirera, Sensors de Gas Semiconductors: Nou mètode d'obtenció de SnO<sub>2</sub> nanocrystal·lí, Research thesis, University of Barcelona, Barcelona (1998).

37. K. D. Scierbaum, U. K. Kirner, J. F. Geiger and W. Göpel, Schottky-barrier and Conductivity Gas Sensors Based upon Pd/SnO<sub>2</sub> and Pt/TiO<sub>2</sub>, *Sensors and Actuators B*, **4**, 87-94 (1991).

38. A. Diéguez, A. Romano-Rodríguez, J. R. Morante, J. Kappler, N. Bârsan and W. Göpel, Nanoparticle engineering for gas sensor optimization: improved sol-gel fabricated nanocrystalline SnO<sub>2</sub> thick film gas sensor for NO<sub>2</sub> detection by calcination, catalytic metal introduction and grinding treatments, *Sensors and Actuators B*, **60**, 125-137 (1999).

39. A. Diéguez, A. Vilà, A. Cabot, A. Romano-Rodríguez, J. R. Morante, J. Kappler, N. Bârsan, U. Weimar and W. Göpel, Influence on the gas sensor performances of the metal chemical states introduced by impregnation of calcinated SnO<sub>2</sub> sol-gel nanocrystals, *Sensors and Actuators B*, **68**, 94-99 (2000).

40. J. Arbiol, P. Gorostiza, A. Cirera, A. Cornet and J. R. Morante, In-situ analysis of the conductance of SnO<sub>2</sub> crystalline nanoparticles in the presence of oxidizing or reducing atmosphere by scanning tunneling microscopy, to be published in *Sensors and Actuators B*.

41. J. Arbiol, P. Gorostiza, A. Cirera, A. Cornet and J. R. Morante, In-situ analysis of the conductance of SnO<sub>2</sub> crystalline nanoparticles in the presence of oxidizing or reducing atmosphere by scanning tunneling microscopy, *Eurosensors 2000 Proceedings and Electronic Extended Abstract*, Copenhagen (2000).

42. J. Arbiol, P. Gorostiza, A. Cirera, A. Cornet and J.R. Morante, In-situ analysis by scanning tunneling microscopy of SnO<sub>2</sub> crystalline nanoparticles, *Second International Conference on Scanning Probe Spectroscopy (SPS 2000)*, Hamburg, (2000).

43. N. Yamazoe, New approaches for improving semiconductor gas sensors, *Sensors and Actuators B*, **5**, 7-19 (1991).

44. N. Yamazoe, Y. Kurokawa and T. Seiyama, Effects of additives on semiconductor gas sensors, *Sensors and Actuators B*, **14**, 283-289 (1993).

45. M. H. Madhusudhana Reddy and A. N. Chandorkar, E-Beam deposited SnO<sub>2</sub>, Pt-SnO<sub>2</sub> and Pd-SnO thin films for LPG detection, *Thin Solid Films*, **349**, 260-265 (1999).

46. A. V. Tadeev, G. Delabouglise and M. Labeau, Influence of Pd and Pt additives on the microstructural and electrical properties of SnO<sub>2</sub>-based sensors, *Materials Science and Engineering B*, **57**, 76-83 (1998).
47. I. Matko, M. Gaidi, J. L. Hazemann, B. Chenevier and M. Labeau, Electrical properties under polluting gas (CO) of Pt- and Pd-doped polycrystalline SnO<sub>2</sub> thin films: analysis of the metal aggregate size effect, *Sensors and Actuators B*, **59**, 210-215 (1999).
48. M. Gaidi, B. Chenevier and M. Labeau, Electrical properties evolution under reducing gaseous mixtures (H<sub>2</sub>, H<sub>2</sub>S, CO) of SnO<sub>2</sub> thin films doped with Pd/Pt aggregates and used as polluting gas sensors, *Sensors and Actuators B*, **62**, 43-48 (2000).
49. B. J. Kip, F. B. M. Duivenvoorden, D. C. Koningsberger and R. Prins, Determination of Metal Particle Size of Highly Dispersed Rh, Ir, and Pt Catalysts by Hydrogen Chemisorption and EXAFS, *Journal of Catalysis*, **105**, 26-38 (1987).
50. S. J. Tauster, Strong Metal-Support Interactions, *Accounts of Chemical Research*, **20** (11), 389-394 (1987).
51. A. Dandekar and M. A. Vannice, Crotonaldehyde Hydrogenation on Pt/TiO<sub>2</sub> and Ni/TiO<sub>2</sub> SMSI Catalysts, *Journal of Catalysis*, **183**, 344-354 (1999).
52. I. Konomi, S. Hyodo and T. Motohiro, Simulation of MEIS Spectra for Quantitative Understanding of Average Size, Composition, and Size Distribution of Pt-Rh Alloy Nanoparticles, *Journal of Catalysis*, **192**, 11-17 (2000).
53. O. Dulub, W. Hebenstreit and U. Diebold, Imaging Cluster Surfaces with Atomic Resolution: The Strong Metal-Support Interaction State of Pt Supported on TiO<sub>2</sub>(110), *Physical Review Letters*, **84** (16), 3646-3649 (2000).
54. S. Bernal, F. J. Botana, J. J. Calvino, C. López, J. A. Pérez-Omil and J. M. Rodríguez-Izquierdo, High-resolution electron microscopy investigation of metal-support interactions in Rh/TiO<sub>2</sub>, *Journal of the Chemical Society, Faraday Trans.*, **92** (15), 2799-2809 (1996).
55. S. J. Tauster, S. C. Fung and R.L Garten, Strong Metal-Support Interactions. Group 8 Noble Metals Supported on TiO<sub>2</sub>, *Journal of the American Chemical Society*, **100**:1, 170-175 (1978).
56. F. Petsy, H-P. Steinrück and T. E. Madey, Thermal stability of Pt films on TiO<sub>2</sub>(110): evidence for encapsulation, *Surface Science*, **339**, 83-95 (1995).
57. R. T. K. Baker, E. B. Prestidge and R. L. Garten, *Journal of Catalysis*, **56**, 390 (1979).

## 5. Metal Ultradispersion

---

58. A.K. Datye, D.S. Kalakkad, M.H. Yao, D.J. Smith, Comparison of Metal-Support Interactions in Pt/TiO<sub>2</sub> and Pt/CeO<sub>2</sub>, *Journal of Catalysis*, **155**, 148-153 (1995).
59. Z. Chang and G. Thornton, Effect of Pd on the interaction of formic acid with TiO<sub>2</sub>(110), *Surface Science*, **459**, 303-309 (2000).
60. G. L. Haller and D. E. Resasco, Metal-Support Interaction: Group VIII Metals and Reducible Oxides, *Advances in Catalysis*, **36**, 173-235 (1989).
61. F. Petsy, H-P. Steinrück and T. E. Madey, Thermal stability of Pt films on TiO<sub>2</sub>(110): evidence for encapsulation, *Surface Science*, **339**, 83-95 (1995).
62. R. T. K. Baker, E. B. Prestidge and R. L. Garten, *Journal of Catalysis*, **56**, 293 (1979).
63. S. J. Tauster, Strong Metal-Support Interactions, *Accounts of Chemical Research*, **20 (11)**, 389-394 (1987).



## 6. Conclusions

---

---

### 6.1 Main Conclusions

The results shown in the present work have demonstrated that the nanoscopic methods applied for the analysis (HRTEM), digital image processing (DIP) and the posterior corroboration of the results obtained by means of computer simulation (CIS), are highly necessary if we want to perform a rigorous study of the SGS materials at the atomic level.

The application of these techniques has allowed us to obtain great results in aspects poorly studied until now. The main part of the works found in literature concerning to SGS materials has been carried out by means of spectroscopic techniques obtaining a general characterization of the samples. In addition, some more studies have been performed in order to analyze the electrical response of the gas sensor device. Nevertheless, there was a need from the nanoscopic point of view in order to determine and analyze the effects of the sensing mechanism at atomic scale.

We have focussed our efforts in determining the general nanoscopic characteristics of the metal additive distribution in semiconductor gas sensor materials. In this way, *Metal Diffusion*, *Superficial Metal Clustering*, *Metal Macro-Agglomeration* and *Metal Ultradispersion* have been widely studied

taking in every case the material system examples most commonly used in SGS field.

The case of *Metal Diffusion* has been observed in the Nb/TiO<sub>2</sub> systems. We have found that Nb diffusion inside TiO<sub>2</sub> anatase bulk hinders both, grain growth and anatase to rutile phase transition. Moreover, we have determined that a maximum of grain growth and phase transition inhibition is given for low Nb loading (at around 3 % Nb at.), while it decreases again for higher loadings. Another important result is that we have been able to relate the Nb segregation out of the TiO<sub>2</sub> anatase structure with the grain growth and phase transition phenomena.

The general phase transition and growth mechanism found has been modeled as follows:

- 1) At the beginning the Nb substitutional ions inhibit the growth and the anatase to rutile phase transition of the grains.
- 2) Once the annealing temperature is increased, Nb is segregated as NbO oxidized species forming nanoclusters on TiO<sub>2</sub> grains surface. Moreover, an important enhancement of the Nb segregation ratio is given when increasing the metal loading percentage due to the higher stress introduced in the anatase structure.
- 3) When Nb in excess is out of the anatase structure, the number of Oxygen vacancies is recovered in order to assure the crystal charge neutrality, favoring the anatase to rutile phase transition. This segregation also assures the reduction of the stress in the TiO<sub>2</sub> structure allowing the grain growth.

*Superficial Metal Clustering* phenomenon has been found in the Pt/TiO<sub>2</sub> systems. The application of nanoscopic techniques has allowed us to determine the morphology and distribution of the Pt metal nanoclusters embedded on TiO<sub>2</sub> surface. We have found that Pt nanoclusters adopt cuboctahedral shape for sizes smaller than 3 nm, and quasi-spherical for sizes bigger than this size (> 3 nm, > 561 atom clusters). Moreover, we have found that the particles analyzed were epitaxially deposited in the following

## 6. Conclusions

---

metal/support relationships:  $[11\bar{1}](011)_{\text{Pt}} \parallel [200](052)_{\text{TiO}_2}$  and  $[001](020)_{\text{Pt}} \parallel [210](\bar{1}20)_{\text{TiO}_2}$ . Furthermore, the implementation of an empirical quantitative method helped us to obtain critical data parameters of crucial importance in sample characterization. The mean number of Pt clusters per  $\text{TiO}_2$  nanograin, the percentage of Pt active atoms (Pt dispersion) and the critical Pt percentage necessary for the merge of the platinum clusters on  $\text{TiO}_2$  grains surface, which it was calculated to be around 7 Pt wt.% in our case.

*Metal Macro-Agglomeration* has been shown as a non-desirable effect common in the case of Pt and Au, since it reduces the total effective area of the nanopowders and decreases the material sensitivity.

Finally, *Metal Ultradispersion* has been found in the Pd/ $\text{SnO}_2$  systems observing two different behaviors depending on the metal loading percentage. In the case of low loading values, the in-situ and ex-situ reducing methods applied, helped us to visualize the ultradispersed Pd atoms when making them sinter into small nanoclusters, even in real-time, in the case of the in-situ method. These reducing methods allowed us to determine the nanoscopic changes when submitting our nanopowders to the SGS working conditions (under reducing environment).

On the other hand, for high Pd loading, we have found that the excess of palladium can influence the  $\text{SnO}_2$  growing, modeling the  $\text{SnO}_2$  nanoparticles to a stick-like structure. This result shows that as well as in the case of Nb on  $\text{TiO}_2$ , metal additives may dramatically influence the semiconductor grain growth evolution. Before reduction Pd nucleates as PdO spherical nanoclusters lying on  $\text{SnO}_2$  surface without epitaxial relationship. Nevertheless, after reduction, PdO clusters are reduced to Pd growing epitaxed on  $\{110\}$   $\text{SnO}_2$  stick-like particles, with the following relationship:  $[1-10](111)_{\text{Pd}} \parallel [001](110)_{\text{SnO}_2}$ .

Our analytical results have been compared with the electrical response of a SGS device obtaining that sensitivity enhancement or inhibition can be directly related to the reduction/oxidation of the noble metal clusters, which would influence in the semiconductors work function by injecting or trapping electrons respectively.

## 6.2 Future Work

Nevertheless, our work does not end here, since thanks to the implementation of the nanoscopic techniques new and highly interesting ways of study have been opened in the SGS materials field.

On one hand, we should complete some of the topics treated in this Ph.D. Thesis work:

- For example, to carry out reducing processes at high temperatures (350 °C) to the SnO<sub>2</sub> samples with high Pd loading, in order to corroborate that the effect of the sensitivity decreasing is really due to the SMSI phenomena. In this way, we should analyze if an encapsulation of the metal nanoclusters by oxide species coming from the semiconductor support occurs.
- To determine the exact Nb loading percentage for which the maximum inhibition of the growing and phase transition is produced in the TiO<sub>2</sub> nanoparticles.
- Or, to corroborate analytical results with electrical measurements of the Gas Sensor Devices implemented with materials studied.

And on the other hand, the most direct application will be the analysis of samples obtained with new and more “exotic” materials and additives, studying the new characteristics and properties they offer:

- In this way, we have started to prepare and characterize new samples made from different semiconductor oxides such as: BaSnO<sub>3</sub>, BaTiO<sub>3</sub>, WO<sub>3</sub>, In<sub>2</sub>O<sub>3</sub>, ... Introducing new metal additives as: Ru, La, Ni,... or other oxide species like Al<sub>2</sub>O<sub>3</sub>.

## 6. Conclusions

---

